

1 **Fractional solubility of iron in mineral dust aerosols over coastal**
2 **Namibia: a link with marine biogenic emissions?**

3
4 **Karine Desboeufs¹, Paola Formenti¹, Raquel Torres-Sánchez^{2,3}, Kerstin Schepanski^{4,\$}, Jean-**
5 **Pierre Chaboureau⁵, Hendrik Andersen^{6,7}, Jan Cermak^{6,7}, Stefanie Feuerstein⁴, Benoit Laurent¹,**
6 **Danitza Klopper^{8,*}, Andreas Namwoonde⁹, Mathieu Cazaunau², Servanne Chevaillier², Anaïs**
7 **Feron^{1,%}, Cécile Mirande-Bret¹, Sylvain Triquet¹, and Stuart J. Piketh⁸**

8
9
10 ¹ Université Paris Cité and Université Paris Est Créteil, CNRS, LISA, F-75013 Paris, France

11 ² Université Paris Est Créteil and Université Paris Cité, CNRS, LISA, F-94010 Créteil, France

12 ³ CIQSO, Robert H. Grubbs Building, University of Huelva, Campus El Carmen, E21071 Huelva, Spain

13 ⁴ TROPOS, Leipzig, Germany

14 ⁵ Laboratoire d'Aérologie (LAERO), Université de Toulouse, CNRS, UT3, IRD Toulouse, France

15 ⁶ Institute of Meteorology and Climate Research, Karlsruhe Institute of Technology (KIT), Karlsruhe,
16 Germany

17 ⁷ Institute of Photogrammetry and Remote Sensing, Karlsruhe Institute of Technology (KIT), Karls-
18 ruhe, Germany

19 ⁸ North-West University, School for Geo- and Spatial Sciences, Potchefstroom, South Africa

20 ⁹ SANUMARC, University of Namibia, Henties Bay, Namibia

21
22 * Now at University of Limpopo, Department of Geography and Environmental Studies, Sovenga,
23 South Africa

24 \$ Now Institute of Meteorology, Freie Universität Berlin, Berlin, Germany

25 % Now at Université Paris-Saclay, INRAE, AgroParisTech, UMR ECOSYS, Palaiseau, France

26
27 **Corresponding author: paola.formenti@lisa.ipsl.fr**

29 **Abstract**

30 ~~Mineral dust is the largest contributor to elemental iron in the atmosphere, and, by deposition, to the~~
31 ~~oceans, where elemental iron is the main growth limiting nutrient. Southern Africa is an important~~
32 ~~source at the regional scale and for the Southern Ocean, however limited knowledge is currently~~
33 ~~available about the fractional solubility of iron from these sources, as well as on the atmospheric~~
34 ~~processes conditioning its dissolution during deposition.~~

35 This paper presents the first investigation of the solubility of iron in mineral dust aerosols ~~from 176~~
36 ~~filter samples~~ collected at the Henties Bay Aerosol Observatory (HBAO), in Namibia, from April to
37 December 2017. During the study period, 10 intense dust events occurred. Elemental iron reached
38 peak concentrations as high as $1.5 \mu\text{g m}^{-3}$, significantly higher than background levels. These events
39 are attributed to wind erosion of natural soils from the surrounding gravel plains of the Namib desert.
40 The composition of the sampled dust is found to be overall similar to that of aerosols from northern
41 Africa, but characterised by persistent and high concentrations of fluorine, which are attributed to local
42 fugitive dust ~~from mining activities and soil labouing for construction.~~

43 The fractional solubility of Fe (%SFe) for both the identified dust episodes and background conditions
44 ranged between 1.3 to 20 % and averaged at 7.9% ($\pm 4.1\%$) and 6.8 ($\pm 3.3\%$), respectively. Even in
45 background conditions, the %SFe iron fractional solubility was correlated to that of aluminium-Al and
46 Silicon. The solubility was lower between June and August, and increased from September on-
47 wards, during the austral spring ~~months~~. The relation with measured concentrations of particulate
48 MSA (methane sulfonic acid), solar irradiance and wind speed suggests a possible two-way interac-
49 tion whereby marine biogenic emissions from the coastal Benguela upwelling to the atmosphere
50 would increase the solubility of iron-bearing dust, according to the photo-reduction processes ~~pre-~~
51 ~~posed by Johansen and Key (2006). The subsequent deposition of soluble iron could act to further~~
52 ~~enhance marine biogenic emissions.~~ This first investigation points to the west coast of southern Africa
53 as a complex ~~and dynamic~~ environment with multiple processes and active exchanges between the
54 atmosphere and the Atlantic Ocean, requiring further research.

55

56 **Keywords:** aerosols, mineral dust, water-soluble Fe, atmospheric processing, marine biogenic emis-
57 sions

58 1. Introduction

59 Through the processes of atmospheric transport and deposition, mineral dust is known to provide
60 nutrients and metals to the terrestrial and marine ecosystems (Hooper et al., 2019; Ventura et al.,
61 2021). Amongst those, mineral dust provides iron (Jickells et al., 2005), which plays a major role for
62 the primary productivity of the nutrient-limited oceans, modulating the marine carbon cycle (Hooper
63 et al., 2019) as well as that of key continental ecosystems such as the Amazon rainforest (Reichholf,
64 1986).

65 To date, much attention has been paid to the soluble Fe in mineral dust emitted from arid and semi-
66 arid areas in the northern Hemisphere, in particular the Saharan and Chinese deserts (e.g. Baker et
67 al., 2006; Paris et al., 2010; Takahashi et al., 2011; Rodriguez et al., 2021), where emissions are the
68 most intense (Tegen and Schepanski, 2009). Nonetheless, the southern Hemisphere accounts for
69 approximately 10% of the global atmospheric dust loading (Kok et al., 2017). Large sources are found
70 in southern Africa, mostly in Namibia (Kalahari and Namib deserts, Etosha Pan, numerous ephemeral
71 riverbeds along the Namibian coastline) and Botswana (Makgadikgadi Pan) (Prospero et al., 2002;
72 Bryant et al., 2007; Mahowald et al., 2003; Ginoux et al., 2012; Vickery and Eckardt, 2013; Von Holdt
73 et al., 2017).

74 Previous research has shown that the long-range transport of dust emitted from southern African
75 sources can reach the south-eastern Atlantic and the Indian Oceans (Swap et al., 1996; Jickells et
76 al., 2005; Bhattachan et al., 2012; 2015; Ito and Kok, 2017). In particular, Gili et al. (2022) demon-
77 strated recently that mineral dust from Namibia can also be transported across the Southern Oceans
78 to eastern Antarctica. Furthermore, the research by Dansie et al. (2022) has suggested that mineral
79 dust from Namibia could dominate the atmospheric deposition to the coastal Benguela Upwelling
80 System (BUS), where biomass burning aerosols, a significant source of soluble Fe to the Southern
81 and Indian Oceans (Hamilton et al., 2021; Ito et al., 2021; Liu, et al., 2022), are limited by atmospheric
82 stratification (Formenti et al., 2019; Redemann et al., 2021). The inputs of Namibian (and Angola)
83 dust in the upwelled waters could also modulate the migration of skipjack tuna between the Gulf of
84 Guinea and the equatorial Atlantic, by contributing to support phytoplankton growth and hence upper
85 trophic levels in this area (Rodriguez et al., 2023).

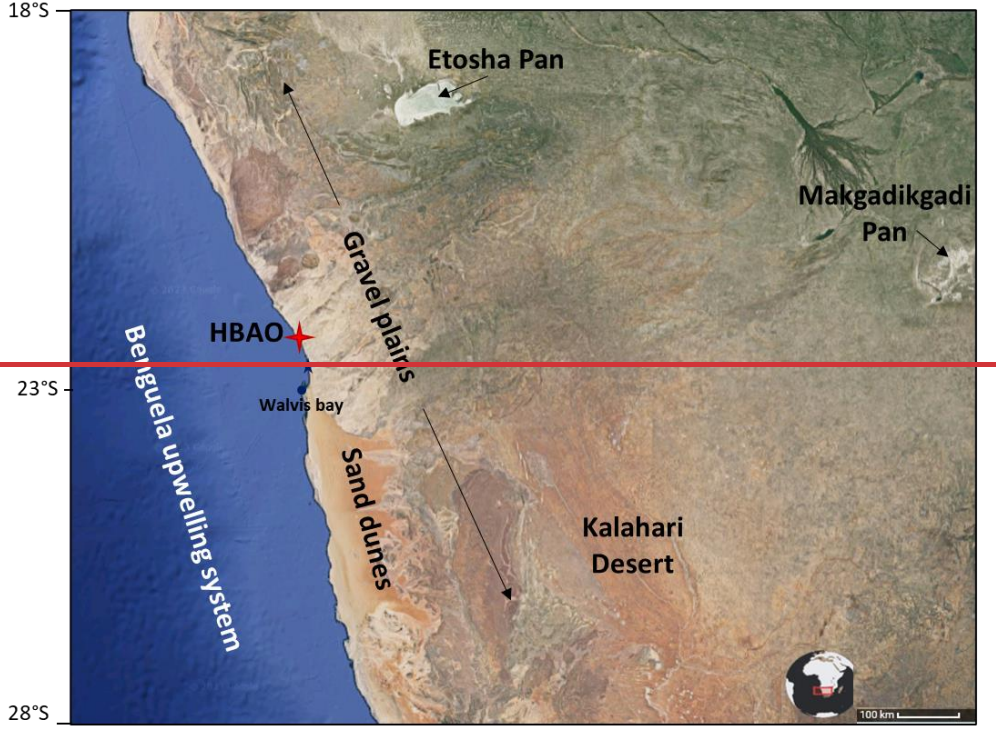
86 There is, however, very little data available on the concentrations and composition of soluble Fe in
87 dust aerosols from southern Africa, both near the sources and over the oceans. Previous research in
88 Namibia focussed on soils and sediments (Dansie et al., 2017a; 2017b; Kanguuehi, 2021). The At-
89 lantic Meridional Transect (AMT) cruise programme conducted recurrent observations between Oc-
90 tober and March in the South Atlantic Ocean (Baker et al., 2013), while Heimbürger et al. (2013) and
91 Gao et al. (2013) report on sparse measurements of deposited aerosols and in rainwaters over the
92 Southern Indian Ocean.

93 Within this context, this paper investigates the fractional solubility of Fe (%SFe) in samples of atmos-
94 pheric aerosol particles smaller than 10 μm in diameter collected in 2017 at the Henties Bay Aerosols
95 Observatory (HBAO; ~~22.09°S, 14.26°E~~) on the Namibian coast. In section 2 we outline the experi-
96 mental and analytical methodology for elemental and water-soluble analysis of ions and metals, in-
97 cluding iron. We also provide the definition of fractional solubility and the method for estimating the
98 total dust mass. We introduce the supporting tools used to evaluate the source regions of the collected
99 mineral dust, their pathways during transport, and the presence of fog, a recurrent feature on coastal
100 Namibia favouring multi-phase ageing processes. Section 3 provides the results of the analysis. We
101 present the iron soluble concentrations and solubility, and explore their links to the load, emission
102 area and transport of mineral dust, as well as atmospheric processing. Section 4 discusses the ob-
103 servations, suggesting that the %SFe fractional solubility of iron in the Namibian dust is higher when
104 the MSA (methane sulfonic acid), a tracer of marine biogenic emissions, is also detected in these
105 highest concentrations. This points to the photo-oxidation of DMS (Dimethyl Sulfide) as a process for
106 increasing the Fe solubility, and suggests a possible positive feedback loop of the iron fertilisation by
107 dust to the ocean. Section 5 summarizes the findings and suggests directions for future research.

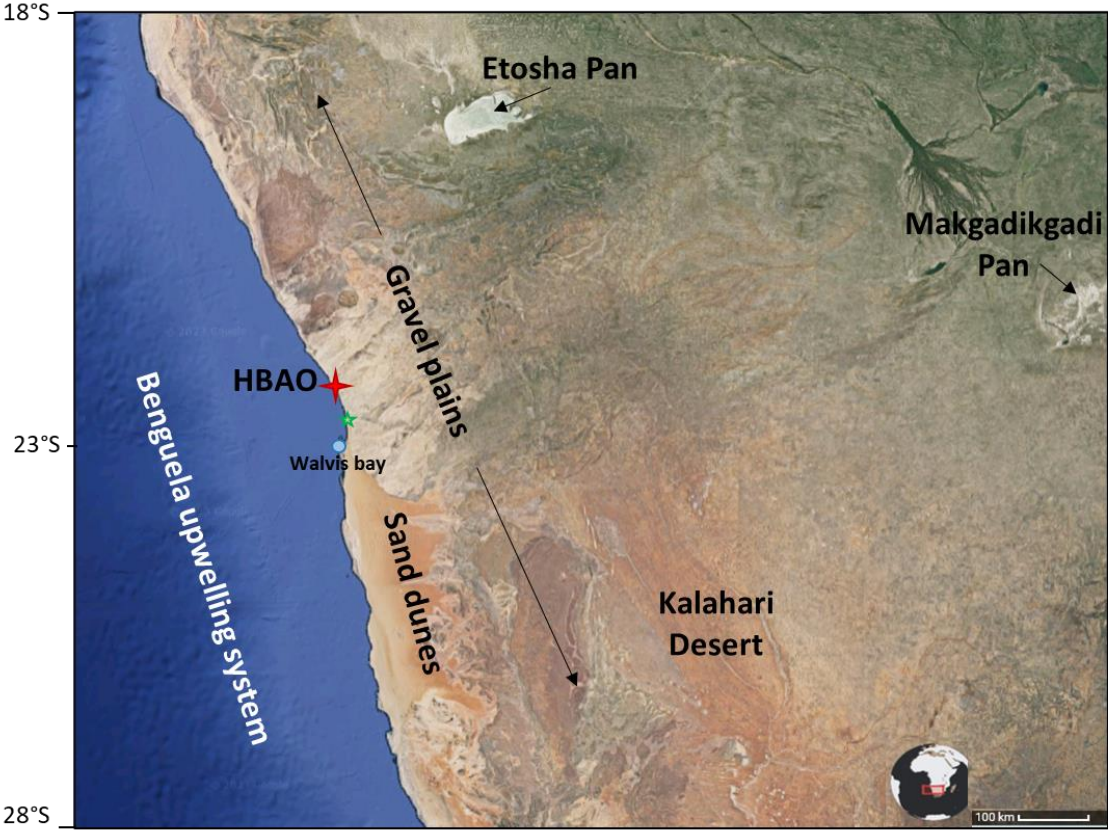
109 2. Methodology

110 2.1. Study area

111 The ~~Henties Bay Aerosol Observatory~~ (HBAO; 22.09°S, 14.26°E; <http://www.hbao.cnrs.fr/>, last ac-
112 cess: 10 October 2022) is located at the Sam Nujoma Marine and Coastal Resources Research Cen-
113 tre (SANUMARC) of the University of Namibia in Henties Bay, Namibia (Fig. 1).



114



115

116 Figure 1: Location of Henties Bay Aerosol Observatory (HBAO, red star) and main dust source regions
 117 (© Google Maps). The position of Walvis Bay (blue dot), the major harbour in the area, and the Wlotzka-
 118 baken meteorological station (blue-green star) are also indicated.

119

120 Three kilometers to the south of the University campus hosting HBAO is the small town of Henties
121 Bay, with no industrial activity and very little traffic, and approximately 170 km north from Walvis Bay,
122 the major harbour in Namibia. Directly east of HBAO are the Namibian gravel plains, which are one
123 of the dominant features of the Namib desert together with the sand dunes. Approximately 100 m to
124 the north is the Omaruru riverbed, one of the coastal sources of mineral dust identified by Vickery and
125 Eckardt (2013).

126 Our previous results show that, at the surface level, the atmosphere at HBAO is a receptor of different
127 air masses dominated by marine aerosols, but also the seasonal occurrence of light-absorbing aero-
128 sols from biomass burning or pollution in northern wind regimes, and mineral dust detected episodi-
129 cally from various wind directions (Formenti et al., 2018; Klopper et al., 2020, hereafter KL20).

130 **2.2. Sample collection and analysis**

131 Aerosol particles smaller than 10 μm in aerodynamic diameter (PM_{10}) were collected by an automated
132 sampler (model Partisol Plus 2025i, Thermo Fisher Scientific, Waltham, MA USA) on 47 mm What-
133 man Nuclepore polycarbonate filters (1- μm pore size). The air was drawn through a certified sampling
134 inlet (Rupprecht and Patashnick, Albany, New York, USA) located at approximately 30 m above
135 ground and operated at a flow rate of 1 $\text{m}^3 \text{h}^{-1}$. Samples were collected for 9 hours during the daytime
136 (from 9:00 to 18:00 UTC time) and night-time (21:00 to 06:00 UTC time) for 12 non-consecutive weeks
137 from April to December 2017 (7-14 April, 26 April-3 May, 19-26 May, 07-14 July, 2-9 August, 15-22
138 August, 18-25 September, 02-09 October, 31 October-7 November, 13-20 November, 28 November-
139 04 December, 12-19 December). In total, 176 samples (+ 13 blanks, one per week of sampling) were
140 collected.

141 The elemental analysis of 24 elements from Na to Pb, ~~and~~ including some major tracers of mineral
142 dust (Fe, Al and Si), was performed at the LISA laboratory by Wavelength-dispersive X-ray fluores-
143 cence (WD-XRF) using a PW-2404 spectrometer (Panalytical, Almelo, Netherlands), as detailed by
144 KL20. The total mass concentration per element x will be referred to as TX.

145 The measured elemental concentrations are used to calculate the estimated dust mass (*EDM*) ac-
146 cording to Lide (1992) as

$$147 \quad EDM = 1.12 \times \{1.658 \times [\text{nss-Mg}] + 1.889 \times [\text{Al}] + 2.139 \times [\text{Si}] + 1.399 \times [\text{nss-Ca}] + 1.668 \times [\text{Ti}] + 1.582$$
$$148 \quad \times [\text{Mn}] + (0.5 \times 1.286 + 0.5 \times 1.429 + 0.47 \times 1.204) \times [\text{Fe}]\} \quad (1)$$

149

150 where, as explained by KL20, nss-Mg and nss-Ca represent the non-sea salt fractions of Mg and Ca,
151 respectively.

152 The analysis of the water-soluble fraction was also performed at LISA. Individual filters were placed
153 in 20 mL of ultrapure water (MilliQ® 18.2 $\text{M}\Omega\cdot\text{cm}$) for 30 minutes. The solution was filtered (Nuclepore

154 polycarbonate filters with 0.2µm pore size) then divided into two sub-samples. One half was analysed
155 by Ion Chromatography (IC) using a Metrohm IC 850 device equipped with a column MetrosepA supp
156 7 (250/4.0 mm) for anions and with a Metrosep C4 (250/4.0 mm) for cations. The IC analysis provided
157 the concentrations of the following water-soluble ions: F⁻, Cl⁻, NO₃⁻, SO₄²⁻, formate, acetate, oxalate,
158 MSA⁻ (methanesulfonic acid), Na⁺, NH₄⁺, K⁺, Ca²⁺ and Mg²⁺. A calibration with certified standard multi-
159 ions solutions of concentrations ranging from 5 to 5000 ppb was performed and the uncertainty of the
160 analysis was estimated to be 5% (KL20).

161 The second half of the solution was acidified to 1% with ultrapure nitric acid (HNO₃) and analysed by
162 Inductively Coupled Plasma-Atomic Emission Spectroscopy (ICP-AES) using a Spectro ARCOS
163 Ametek® ICP-AES and by High-resolution Inductively Coupled Plasma-Mass Spectrometry (HR-ICP-
164 MS) using a Neptune Plus™ instrument by Thermo Scientific™. The calibration curve was performed
165 using standard multi-element solutions ranging from 2 to 1000 ppb for ICP-AES and 1 to 1000 ppt for
166 HR-ICP-MS (Desboeufs et al., 2022). These analyses provided the dissolved mass concentrations
167 (DX) of 25 water-soluble metals and metalloids, including Fe, Al, and Si. All sample concentrations
168 were corrected using the filter blanks for each sampling period.

169 Based on those analyses, the fractional solubility (%SX) representing the percentage solubility value
170 was calculated as

171

$$172 \qquad \qquad \qquad \%SX = 100 \times DX/TX \qquad \qquad \qquad (2)$$

173

174 with DX and TX, the dissolved and total elemental concentration respectively.

175 Here, a leaching protocol using ultrapure water (UPW) was used to simulate wet deposition of parti-
176 cles, since the wet deposition dominates the total iron supply in the Southern Atlantic Ocean (Chance
177 et al., 2015). Moreover, the UPW leach enables the chemical reaction between iron with organic or
178 inorganic ligands, naturally dissolved from the particulate aerosols into rain droplets. However, it is
179 known that the extraction protocol modulates dissolution process and hence the values of ~~%SFe_{iron}~~
180 ~~fractional solubility~~, in particular the estimates using UPW are higher in comparison to these one using
181 seawater, but lower than the acidic, buffered or reduction agent leach (Perron et al., 2020).

182 **2.3. Ancillary data**

183 Maps of the emission fluxes of mineral dust were calculated using the dust emission model described
184 by Feuerstein and Schepanski (2019), driven with hourly 10m wind fields at a 0.1° x 0.1° grid from
185 the European Centre for Medium-range Weather Forecasts (ECMWF). The dust emission parame-
186 terisation follows Marticorena and Bergametti (1995). Additional information on the soil type was taken

187 from the ISRC soil data set (FAO/IIASA/ISRIC/ISSCAS/JRC, 2012) and information on the aerody-
188 namic roughness length was obtained from POLDER/ADEOS surface products following the works
189 of Marticorena et al. (2004) and Laurent et al. (2005). The MODIS monthly vegetation product
190 (MYD13A3 v6) was used to describe the vegetation cover, while the vegetation type was defined
191 using the BIOME4 database (Kaplan et al., 2003). We additionally differentiated between different
192 dust source types (alluvial fines, dunes and sand sheets) which allowed us to reflect the source di-
193 versity over Namibia and thus the spatial diversity in the soil's susceptibility to wind erosion. This layer
194 was compiled following Feuerstein and Schepanski (2019) using MODIS surface reflectance
195 (MOD09A1 v6). A MODIS retrieved map on surface water cover was used to eliminate flooded areas
196 as active dust sources.

197 Back-trajectories of the air masses during the dust events were calculated from Meso-NH model (ver-
198 sion 5.3). The model set-up is similar to the one used for the AErosols, RadiatiOn and CLOuds in
199 southern Africa (AEROCLO-sA) field campaign (Formenti et al. 2019) and related case studies (Fla-
200 mant et al. 2022; Chaboureau et al. 2022). In short, the model was run on a 5 km grid covering the
201 southern tip of Africa and 67 stretched levels spaced by 60 m close to the surface and 600 m at high
202 altitude. Meso-NH was run for 24 h for each dust event using initial and boundary conditions provided
203 by the ECMWF operational analysis. Emission, transport and deposition of dust is described by the
204 scheme of Grini et al. (2006). Back trajectories were computed online using three passive tracers
205 initialized with the 3D-field of their initial conditions. Further details on the dust prognostic scheme,
206 the backward trajectories and the physical parameterizations are given in Chaboureau et al. (2022).

207 The presence of fog and low clouds (FLC) along the Namibian coastline during dust events was an-
208 alysed using an existing satellite-based fog and low-cloud data set (Andersen et al., 2019). The FLC
209 detection algorithm used to create this data set was developed and validated specifically for this re-
210 gion. The algorithm is based on infrared observations from the Spinning Enhanced Visible and Infra-
211 red Imager (SEVIRI) aboard the geostationary Meteosat Second Generation (MSG) satellites, making
212 use of both spectral and textural information. The FLC product is available at the native spatial and
213 temporal resolutions of the SEVIRI sensor (3 km nadir, every 15 minutes), as described in Andersen
214 and Cermak (2018). The FLC product does not specifically distinguish between fog and low clouds
215 but captures the coastal boundary-layer cloud regime typical for the region and at HBAO that could
216 interact with mineral dust. It has been shown to be consistent with synoptic-scale atmospheric dy-
217 namics (Andersen et al. 2020). The FLC data are used to calculate maps of average fog and low
218 cloud coverage for the time periods of all dust events given in Table 1.

219 Observations of the local meteorology, including measurements of air temperature, relative humidity
220 and fog, at the nearby Wlotzkasbaken meteorological station (22.31°S, 14.45°E, 73 m asl, see Fig.

221 1) part of the Southern African Science Service Centre for Climate Change and Adaptive Land Man-
 222 agement (SASSCAL) ObservationNet (<https://www.sasscal.org/>; last accessed 14/04/2023), are
 223 used.

224

225 3. Results

226 3.1. Description of the dust episodes

227 The dataset discussed in this paper is based on 176 aerosol samples collected at HBAO, 42 of which
 228 were associated with 10 dust episodes. As detailed by KL20, events of mineral dust were identified
 229 as peaks in the time series of the mass concentrations of Al and non-sea-salt Ca^{2+} (nss- Ca^{2+}). The
 230 dust episodes investigated in this study are a subset of those presented by KL20, we therefore use
 231 their naming convention to facilitate the connections between the two papers (Table 1). In the follow-
 232 ing, we refer to samples collected during the dust episodes as “dust”. Samples collected outside the
 233 dust events will be indicated as “background”.

234

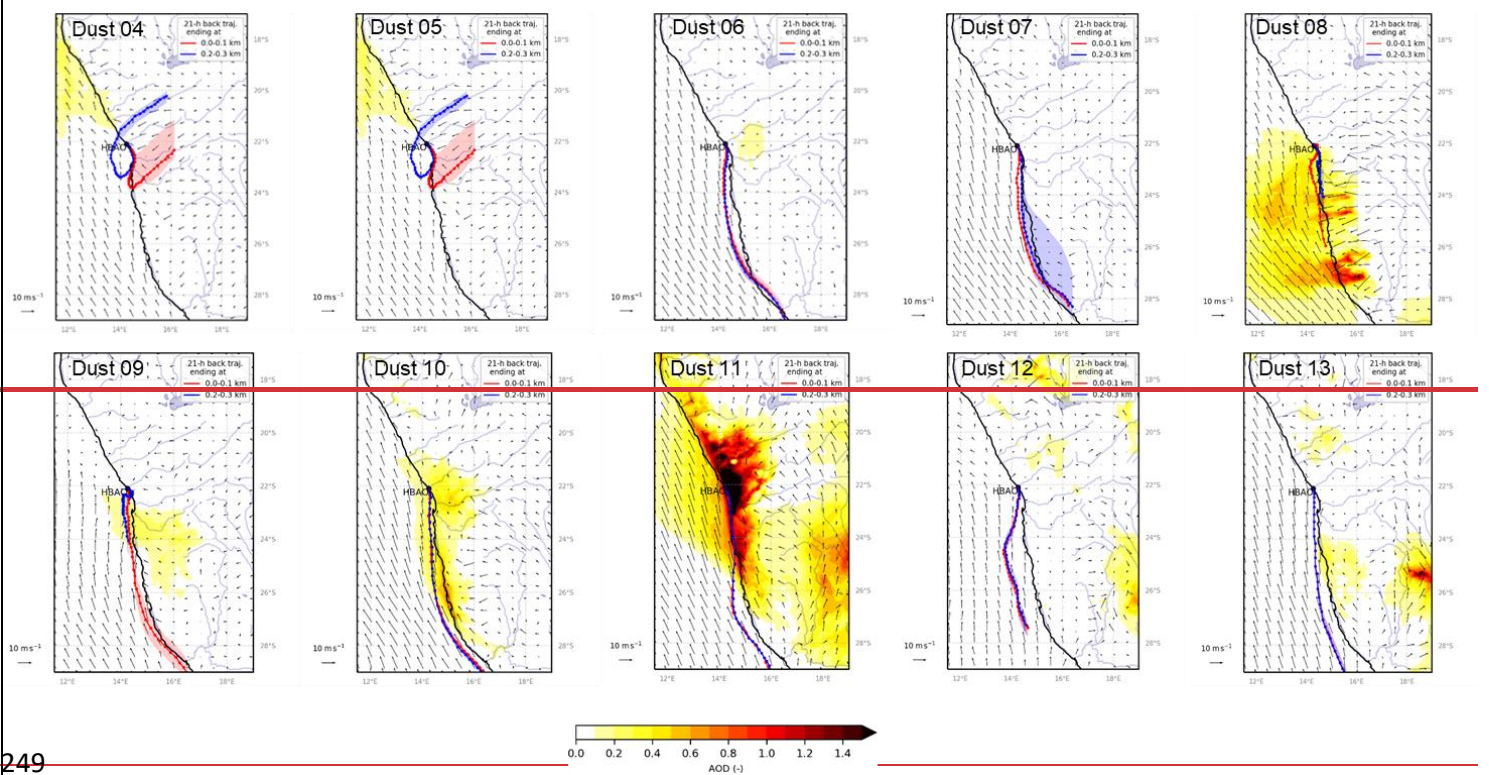
235 **Table 1.** Dates of dust events identified at HBAO from May to December 2017, following KL20. The number of
 236 samples collected during each episode is indicated in the column called “N”. The average air temperature,
 237 relative humidity, wind speed and direction recorded at the nearby meteorological station in Wlotzkasbaken are
 238 reported. The maxima wind speed and corresponding direction are indicated in brackets in the corresponding
 239 columns. The average EDM is reported with in brackets the maximum of EDM during the event.

Episode identifier	Start and end date (UTC)	N	Air temperature (°C)	RH (%)	Wind speed (m s ⁻¹)	Wind direction (degN)	EDM (µg m ⁻³)
Dust 04	19/05 09h – 20/05 18h	3	17.7	73.7	2.7 (6.2)	186 (185)	13 (14)
Dust 05	24/05 21h – 26/05 09h	3	18.1	63.3	2.3 (6.3)	183 (188)	21 (42)
Dust 06	11/07 09h – 13/07 09h	4	13.2	82.9	1.2 (5.4)	235 (193)	27 (45)
Dust 07	04/08 21h – 06/08 09h	4	12.5	87.0	1.2 (5.4)	233 (201)	10 (16)
Dust 08	17/08 21h – 19/08 09 h	4	11.9	80.6	1.3 (4.6)	324(129)	18 (21)
Dust 09	23/09 21h – 24/09 18h	2	15.6	84.3	3.1 (6.2)	309 (330)	11 (17)
Dust 10	05/10 21h – 08/10 09h	8	14.0	74.6	2.1 (5.9)	249 (228)	14 (23)
Dust 11	15/11 09h – 18/11 09h	6	16.7	66.1	3.2 (11.7)	231 (232)	31 (56)
Dust 12	30/11 09h – 01/12 18h	3	16.7	78.1	1.9 (5.7)	244 (195)	2 (3)
Dust 13	15/12 09h – 19/12 09h	7	16.9	76.9	2.9 (6.5)	252 (238)	10 (19)

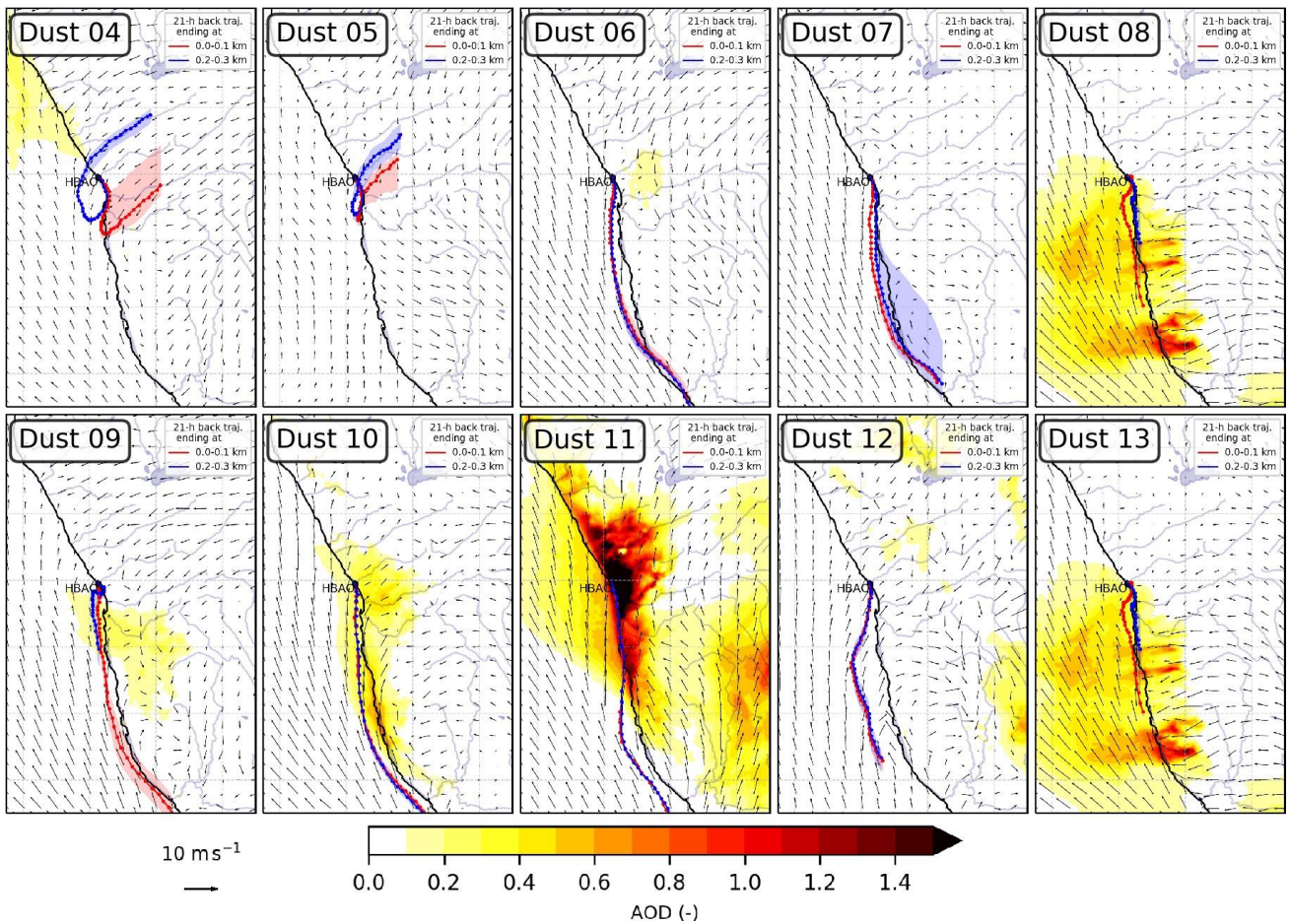
240

241 The dust episodes were long-lasting (generally a few days). The dynamic of the emissive areas, air
 242 mass transport and fog coverage during the episodes (Fig. 2 and S1) is driven by the synoptic circu-
 243 lation, which, in southern Africa, is primarily affected by the high-pressure belt under the descending
 244 limb of the Hadley cell (Tyson and Preston-Whyte, 2014). The maps of dust emission fluxes and the
 245 air mass back-trajectories reflect this seasonality. During the first part of the year (episodes Dust 04

246 to 05), dust emissions originated from the gravel plains and the Etosha pan north of HBAO. During
247 this time of the year the transport to HBAO below 300 m asl was north- to south-easterly originating
248 inland from the coast.



249



250
 251 **Figure 2:** Maps of dust optical depth (shading) and 10-m wind (vector) overlaid by pathway of 21-hour
 252 air mass back trajectories ending in the first 100 m (red line) and between 200 and 300 m (blue line)
 253 above HBAO for dust episodes, as calculated by the Meso-NH model (version 5.3). Dots are plotted
 254 every hour and shadings around these lines are the interquartile ranges for latitudes.

255
 256 From July onwards, the active source areas were identified in the southern gravel plains, Namib sand
 257 dunes and Kalahari Desert (this former source only for Dust 11 to 13). Air mass transport was south-
 258 erly and travelled over the sea and along the coastline. It is worth noticing that all the air masses
 259 experienced maritime air during their last hours of transport, including the episodes Dust 04 and 05
 260 associated with berg wind conditions, due to the coastal low that develops to the west of HBAO.

261 The formation of fog events at Henties Bay is also highly seasonal. The frequency of occurrence of
 262 fog events is highest during austral winter at the coast, whereas lifted stratus clouds dominate during
 263 austral summer, when overall FLC occurrence peaks. The occurrence of fog over Namibia correspond
 264 to the advection of low-level clouds which is modulated both by local meteorology along the coastline
 265 of Namibia (trade winds) and synoptic-scale radiative processes (Spirig et al., 2019; Andersen et al.,
 266 2019; 2020). Henceforth, as shown in Fig. S1, the presence of fog and low clouds correlates with
 267 wind directions and aerosol source regions. Overall, three episodes (Dust 04, Dust 05 and Dust 11 in
 268 April, May and November, respectively) occurred in fog-free or low-fog conditions. The remaining
 269 episodes were characterised by extensive fog and low cloud coverage throughout the study area. The

270 meteorological observations at the nearby Wlotzkasbaken station (Fig. S2) confirm these findings,
 271 and show in particular that the relative humidity always exceeded 60 %, and 80 % when fog or low
 272 clouds were present (Table 1). As a consequence, the aerosol can be considered deliquescent even
 273 in the fog-free conditions. The seasonality is also observed in the average downwelling solar irradi-
 274 ance, with the lowest values during July and September, associated with austral winter. Finally, it is
 275 interesting to note that the fog-free conditions, associated with the predominance of continental air
 276 masses, corresponded to the highest ~~estimated dust mass (EDM)~~, possibly because of the reduced
 277 wet removal during transport and the increase of emission fluxes with the decrease of soil moisture
 278 (Kok et al., 2014), but possibly also because of the high wind speed prevailing during these conditions,
 279 which in principle, enhances both dust emissions and transport (Table 1).

280 3.2. Iron solubility

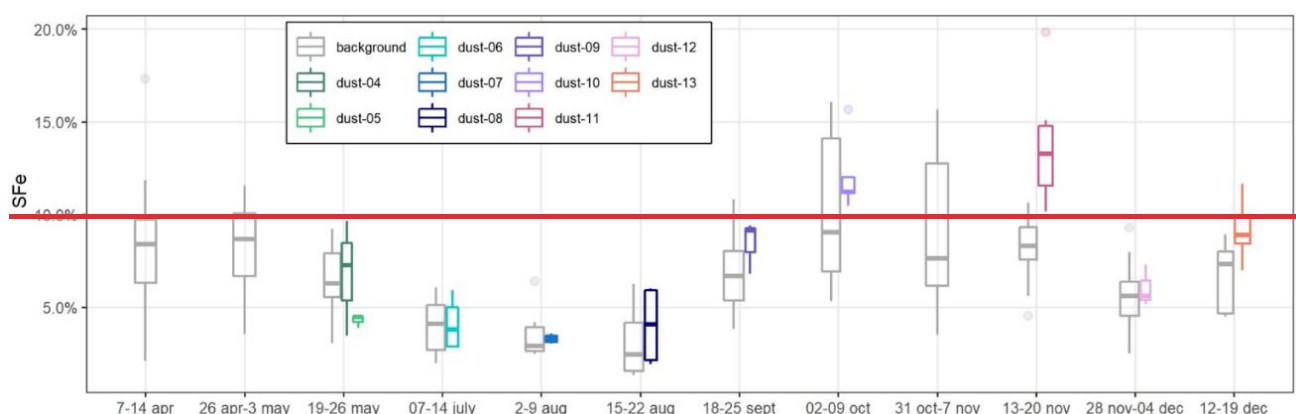
281 The total and dissolved concentrations, and fractional solubility of Fe, Al and Si, during the dust epi-
 282 sodes are reported in Table 2, where they are compared to background conditions. For iron, the
 283 average values over the entire sampling period are also shown.

284 **Table 2.** Average and standard deviations of water-soluble (DX), total elemental (TX) mass concentrations and
 285 fractional solubility (%SX) for Fe, Al and Si at HBAO measured for the total period and during the dust and
 286 background events from April to December 2017. Concentrations values are expressed in ng m^{-3} , while frac-
 287 tional solubility is expressed in percent. The numbers of considered samples is presented between the paren-
 288 theses.

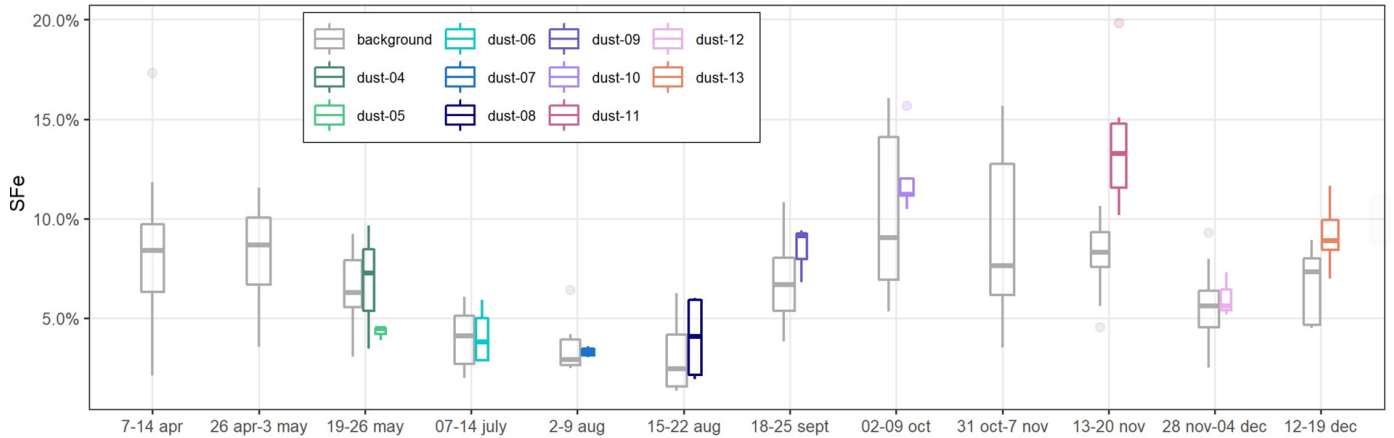
	Fe			Al		Si	
	All period	Dust	Background	Dust	Background	Dust	Background
DX	28 ± 51 (N=175)	80 ± 84 (N=42)	11 ± 10 (N=131)	322 ± 296 (N=42)	56 ± 46 (N=131)	529 ± 616 (N=42)	78 ± 83 (N=124)
TX	364 ± 482 (N=176)	955 ± 633 (N=42)	177 ± 155 (N=133)	1204 ± 870 (N=42)	284 ± 222 (N=94)	4158 ± 3037 (N=42)	776 ± 674 (N=133)
%SX	7.1 ± 3.6 (N=175)	7.9 ± 4.1 (N=42)	6.8 ± 3.3 (N=130)	27 ± 10 (N=42)	26 ± 11 (N=90)	12 ± 7 (N=42)	11 ± 8 (N=116)

289
 290 The total Fe concentrations varied significantly from one episode to the other, and so did EDM, which
 291 was larger than $10 \mu\text{g m}^{-3}$ for all of them (except Dust 12) and as high as $56 \mu\text{g m}^{-3}$ during Dust 11
 292 event (Table 1). By contrast, the total Fe-to-EDM ratio was virtually constant, with an average of 5.8
 293 % (± 0.6 %) for the dust events and 5.6 % (± 1.1 %) for the entire dataset. These values are quite
 294 superior to usual Fe content recommended in upper continental crust models (3.5% for Taylor and
 295 McLennan or 5.04 ± 0.53 % Rudnick and gao, 2004) and estimated in Saharan dust (4.45% for
 296 Guieu et al., 2002; 4.3 to 6.1% for Lafon et al., 2006 or 4.5% for Formenti et al., 2008). Keeping in
 297 mind that Fe abundance is estimated, this suggests that the Namibian aerosol dust could be enriched
 298 in iron in comparison to upper crust and dust provided by Saharan sources.

299 The total dissolved concentrations of Fe during the sampling period ranged from 1.5 to 427 ng m⁻³,
 300 with a median and average of 10.5 and 28 ng m⁻³. During the dust episodes, the average mass con-
 301 centration of dissolved Fe was 80 ± 84 ng m⁻³, almost an order of magnitude higher than for back-
 302 ground conditions (11 ± 10 ng m⁻³). The dissolved concentrations in dust periods are higher than
 303 those observed in the South Atlantic Ocean for air masses associated with transport from continental
 304 southern Africa (Baker et al., 2013; Chance et al., 2015; Baker and Jickells, 2017), which are of the
 305 order as those observed at HBAO for background periods. The calculated ~~%SFe iron fractional solubility~~
 306 ~~of Fe~~ ranged from 1.3 to 19.8 %, with a median and average of 6.7 and 7.1 %. The average %SFe
 307 during dust events (7.9 ± 4.1%) was higher, but quite similar than in background conditions (6.8 ±
 308 3.3%). It is interesting to note that Dust 11 event, the most intense recorded event, presents the
 309 highest %SFe (between 10.2 and 19.8 % with an average at 13.8 %). Apart from this event, the
 310 average fractional solubility seems to be independent of the EDM. Excluding this event, the average
 311 solubility of Fe for dust events (6.9 % ± 3.3 %) is equivalent to the one for background samples. The
 312 uniformity of ~~%SFe iron solubility~~ values between background and dust periods contrasted with the
 313 observations made in regions where the dust influence is sporadic and the origin of Fe is associated
 314 to various sources (e.g. Shelley et al., 2018). That is consistent with a main dust source of iron in our
 315 samples, as indicated in KL20. For both conditions, the observed range of variability is high and con-
 316 sistent with previous observations over the Southern Atlantic Ocean (2.4-20 %, Baker et al., 2013;
 317 1.3-22 %, Chance et al., 2015), and the Southern Indian Ocean (0.76-27 %, Gao et al., 2013), using
 318 acetate buffer leach at pH 4.7 (0.4µm) which can extract 1.4 times more Fe than UPW protocol (Per-
 319 ron et al., 2020). Moreover, the measured ~~%SFe iron fractional solubility~~ is significantly higher than
 320 obtained from dissolution experiments, with an identical protocol, of mineral dust aerosol samples
 321 collected on filters after laboratory generation from the soils collected in Namibian sources (< 1%;
 322 Formenti et al., in preparation, 2024).



323



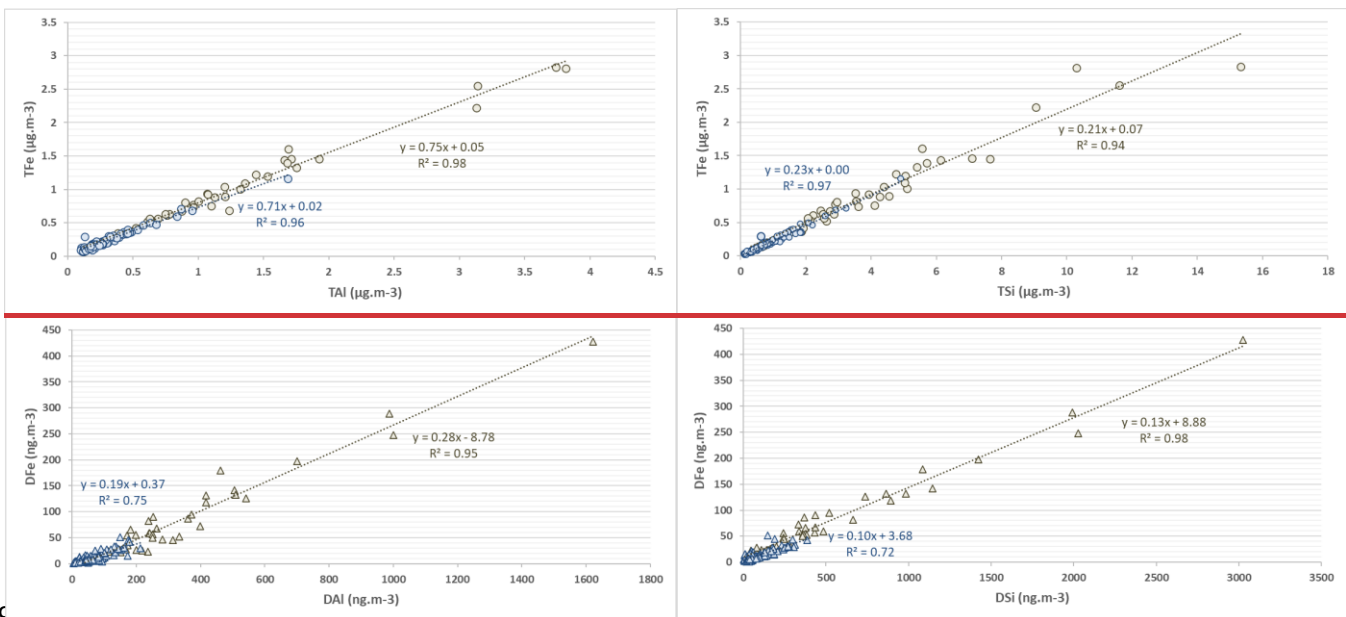
324

325

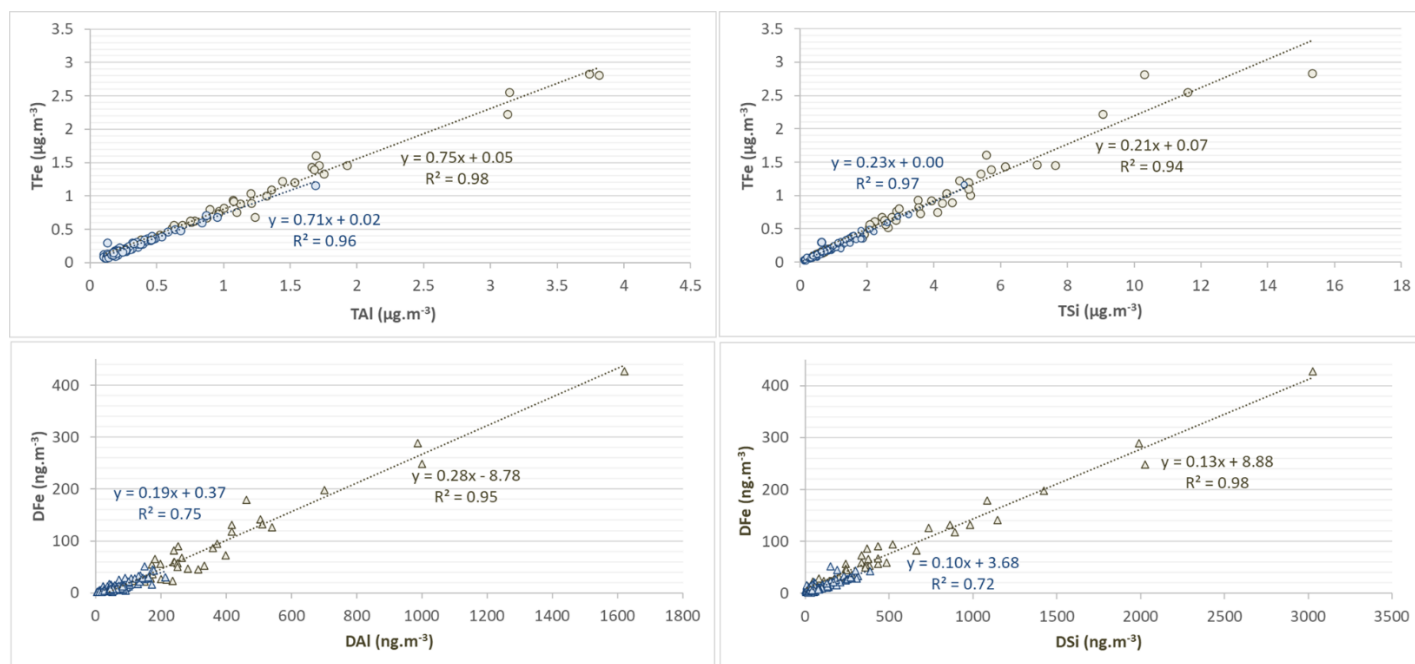
326 **Figure-3**: Temporal variability of %SFe average for dust and background samples during the different
 327 periods of sampling. In the box plots, the box indicates the interquartile range, i.e. the 25th and the 75th
 328 percentile, and the line within the box marks the median. The whiskers indicate the quartiles ± 1.5 times
 329 the interquartile range. Points above and below the whiskers indicate outliers outside the 10th and 90th
 330 percentile.

331

332 The temporal variability of %SFe is presented in Fig. 3, where dust and background episodes are
 333 shown separately. The temporal variability is similar during dust and background conditions. The
 334 highest %SFe occurred during austral spring (October-November), and in particular during episode
 335 Dust 11 from 13 to 20 November 2017, when the average %SFe reached 13.8 %. The %SFe was
 336 quite similar along the year between dust and background, except between 13-20 November where
 337 the iron solubilities during Dust 11 event was very superior to the one of background samples, and to
 338 a lesser extent, in September (Dust 09) and December (Dust 13).



339



340
 341 **Figure 4:** Scatterplot of TFe with respect to TAl and TSi (top panels) and DFe with respect to DAl and
 342 **DSi** (bottom panels) for dust (sand dots and triangles) and background events (blue dots and triangles).
 343 The Pearson coefficient are shown for both.

344

345 Figure 4 represents the correlations of Fe with Al and Si, both for the total and the dissolved concen-
 346 trations. For both dust and background samples, the total Fe concentration is linearly correlated with
 347 total Al ($R^2=0.98$ and 0.96 , slope= 0.75 and 0.71 , for dust and background conditions respectively)
 348 and total Si ($R^2=0.94$ and 0.97 , slope= 0.21 and 0.23 , respectively). The slopes are consistent with
 349 typical Fe/Al and Fe/Si ratios found in desert dust from northern Africa (Formenti et al., 2011; Shelley
 350 et al., 2014), confirming the main crustal origin of Fe during all the sampling periods. Likewise, the
 351 concentrations of dissolved iron (DFe) show a strong linear correlation with both DAl and DSi, for both
 352 for dust and background events ($R^2=0.96$ and 0.75 with respect to DAl and $R^2=0.98$ and 0.73 with
 353 respect to DSi). The slopes for Al and Si are also comparable (0.19 and 0.28 for DAl and 0.10 and
 354 0.13 for DSi, respectively in dust and in background events). A very strong linear correlation was also
 355 observed between DFe and DTi ($R^2=0.96$ and 0.84 ; not shown), another unique marker of mineral
 356 dust. Significant correlations of soluble concentrations for several elements associated with mineral
 357 dust (Fe, Al, Si, Ti) have been previously obtained in remote aerosols over oceanic areas (Baker et
 358 al., 2016). Additionally, DFe during dust events correlate very closely with F^- ($R^2=0.94$, not shown),
 359 which has been indicated by KL20 as being emitted in the atmosphere by the wind erosion as well as
 360 the labouring of the Namibia soil, rich in fluoride mineral deposits.

361 4. Discussion

362 Several studies have shown that variations in aerosol Fe solubility could result from the
 363 source/composition of the aerosols. As a matter of fact, the Fe solubility has been linked to the iron

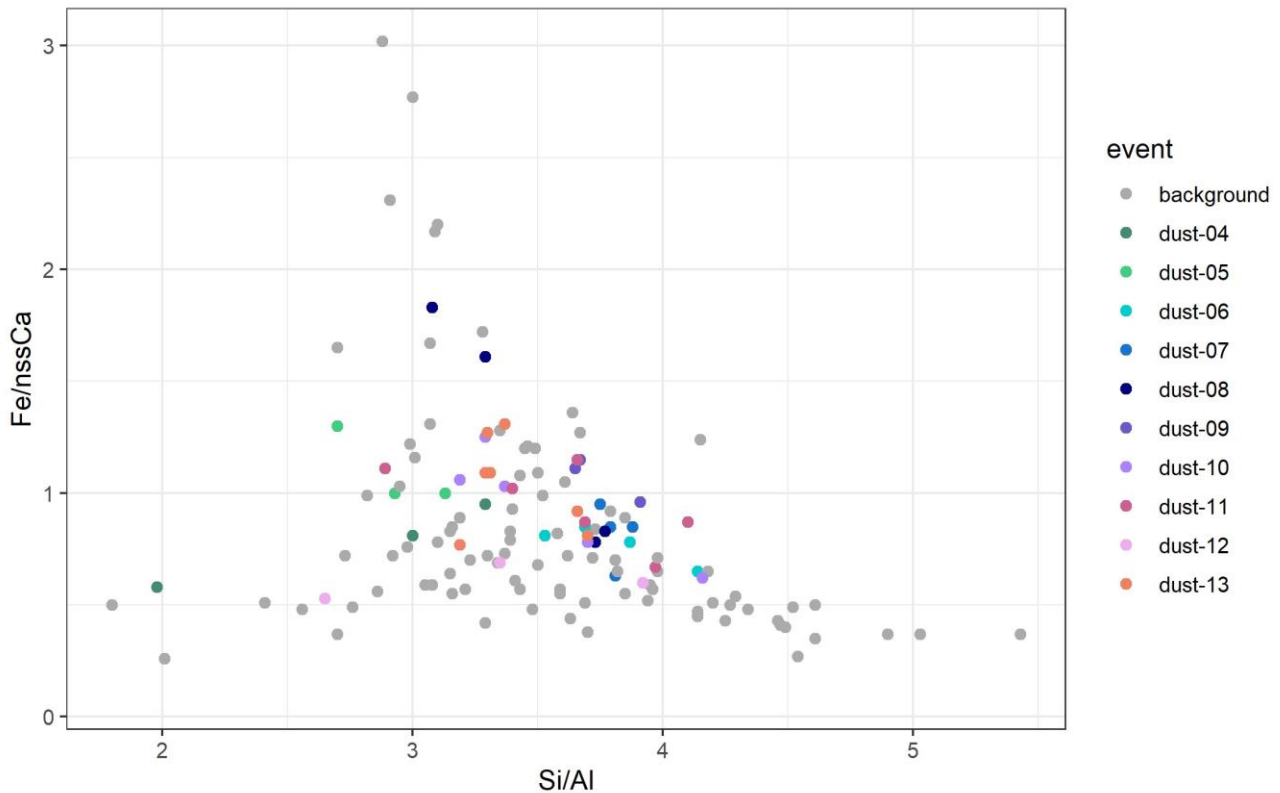
364 mineralogy (Journet et al., 2008) and has been shown being lower for African crustal sources than in
365 continental/anthropogenic sources (Desboeufs et al., 2005; Sholkovitz et al., 2009; Shelley et al.,
366 2018). The iron fractional solubility in mineral dust is also affected by source mixing (Paris et al., 2010;
367 Desboeufs et al., 2005), by (photo)chemical processing with acids or organic ligands during atmos-
368 pheric transport (Paris et al., 2011, Paris et Desboeufs, 2013; Wozniak et al., 2013; Swan and Ivey,
369 2021) and by the increase of surface area to volume ratio due to size changes during transport (Baker
370 & Jickells, 2006; Marcotte et al., 2020).

371 In the following sections, we discuss these possible factors to explain the seasonality and the ex-
372 tended range of variability of the ~~fraction-Fe-solubility~~%SFe in HBAO samples. The possible increase
373 of surface area to volume ratio during transport (Baker and Jickells, 2006; Marcotte et al., 2020) will
374 not be discussed because of lack of appropriate observations of the size distribution. Because of the
375 similar transport time suggested by back trajectories (Fig. 2), it is likely that particle size distribution
376 would be similar from one event to the other.

377 **4.1. Influence of dust composition**

378 Close to the dust source, iron solubility could be mainly conditioned by the mineralogical composition
379 of dust (Journet et al., 2008, Formenti et al., 2014). Considering that soluble Fe-bearing aerosols were
380 issued from mineral dust for all the samples, the seasonality of dust emission sources (see 3.1) could
381 be a factor explaining the seasonality of %SFe (and other elements associated to mineral dust).
382 Figure 5 shows the scatter plot of the elemental mass ratio of Fe/nss-Ca²⁺ and Si/Al, previously used
383 for northern Africa dust to distinguish aerosol dust from source areas enriched in clays or iron oxides
384 to soils rich in quartz or carbonates (Formenti et al., 2014). Specific to Namibia, because of the strong
385 link between nss-Ca²⁺ and fluorine, the Fe/nss-Ca²⁺ ratio may also to distinguish dust influenced by
386 fluorspar mining.

387



388

389 **-Figure 5-: Scatterplot of Fe/nss-Ca^{2+} and Si/Al mass ratios for the samples collected at HBAO in period**
 390 **May-December 2017. Values obtained for samples collected during the dust events are represented as**
 391 **colored dots. Values for samples collected outside those events (background) are represented as grey**
 392 **dots.**

393

394 Figure 5 indicates that the range of variability of both Fe/nss-Ca^{2+} and Si/Al ratios is small when con-
 395 sidering dust events only. The elemental ratios of samples collected during the background periods
 396 are rather similar to dust events during a same sampling period, except for Si/Al for the period be-
 397 tween 19-26 May and for Fe/nss-Ca^{2+} for the samples of 18-25 September, when significant differ-
 398 ences, not really explicable and not inducing a significant difference in the %SFe values are observed
 399 (Fig. S3).

400 The values for ambient dust measured at HBAO are consistent with those of the previous field obser-
 401 vations in Namibia (Annegarn et al., 1983; Eltayeb et al., 1993), but also with values reported by
 402 Caponi et al. (2017) for laboratory-aerosolised dust from two soils collected on the Namibian gravel
 403 plains. This is in agreement of the indications of the emission maps (Fig. 2), showing significant emis-
 404 sions in the gravel plains. The absence of seasonal cycle in the elemental composition illustrated in
 405 Figure S3 suggests that the seasonal change from northern to southern sources does not induce a
 406 change in the composition of the aerosol dust sampled at HBAO, which is consistent with the fact that
 407 the northern and the southern gravel plains of Namibia have similar mineralogy (Heine and Vökel,
 408 2010). This suggests that the mineralogical composition of mineral dust should not be a discriminating
 409 factor explaining the seasonality of the iron solubility observed at HBAO.

410 4.2. Evidence of processing by marine biogenic emissions

411 The atmospheric (in-cloud) processing associated with secondary aerosol production may increase
412 the fractional solubility of Fe during transport (Takahashi et al., 2011; Rodríguez et al., 2021). This
413 has also been shown for Al and Ti (Baker et al., 2020). The chemical processing could include both
414 acidic and ligand-promoted dissolution (Desboeufs et al., 2001, Longo et al., 2016, Tao et al., 2019).
415 Oxalic acid has previously been used as a proxy for organic ligand-mediated iron dissolution pro-
416 cesses because it is the most abundant species in the atmosphere and is the most effective ligand in
417 promoting iron dissolution (Baker et al., 2020; Hamilton et al., 2021). However, several secondary
418 compounds, such as carboxylate ligands and marine secondary products derived from **dimethyl sul-**
419 **fide (DMS)** oxidation, have been identified as playing a role in increasing the soluble fraction of iron
420 from mineral aerosols (Johansen and Key, 2006; Paris et al., 2011; Paris and Desboeufs, 2013; Woz-
421 niak et al., 2013 and 2015). The increase of ligands-promoted dissolution is attributed to photochem-
422 ical reduction of Fe(III) in Fe (II) (Siefert et al., 1994; Johansen and Key, 2006).

423 To investigate these aspects, the mass concentrations of the ionic compounds (oxalate, formate,
424 MSA, NO_3^- , NH_4^+ and nss-SO_4^{2-}) implied in the secondary aerosol production, measured at HBAO
425 during dust and background periods are reported in Table 3.

426

427 **Table 3.** Average and standard deviations of mass concentrations of water-soluble ions measured at HBAO during dust and
428 background events from May to December 2017. Concentrations are expressed in ng m^{-3} . The number of samples pertaining
429 to each occurrence is indicated in brackets.

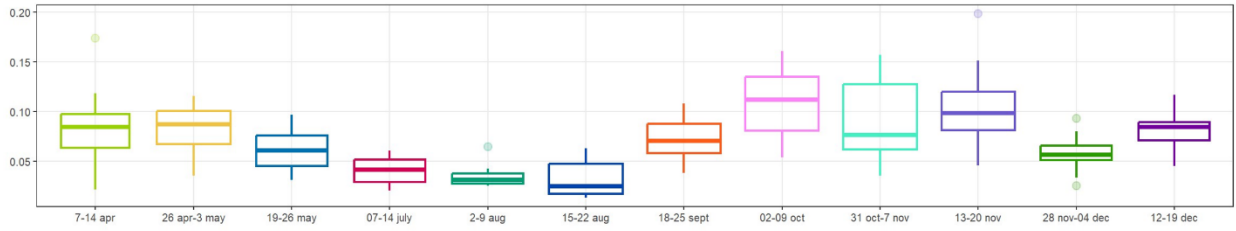
	Dust	Background
nss-SO_4^{2-}	1795 ± 762 (N = 42)	1366 ± 505 (N=132)
Oxalate	155 ± 53 (N = 42)	127 ± 35 (N = 132)
Formate	18 ± 6 (N = 40)	16 ± 9 (N = 105)
MSA	64 ± 37 (N=36)	56 ± 36 (N=114)
NO_3^-	205 ± 79 (N=42)	200 ± 138 (N=132)
NH_4^+	192 ± 71 (N=42)	207 ± 98 (N=132)

430

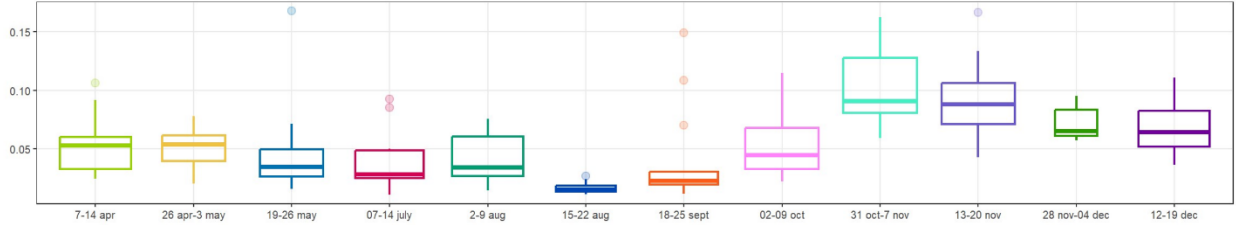
431 Oxalate was the most abundant organic compound, followed by MSA, a secondary product of DMS
432 oxidation and a unique particulate tracer of the primary marine biogenic activity (Andreae et al., 1995).
433 On average, organic compounds were equally concentrated in dust and background events. Amongst
434 inorganic species, nss-SO_4^{2-} was the most concentrated compound, with higher values during the
435 dust events than during the background period.

436

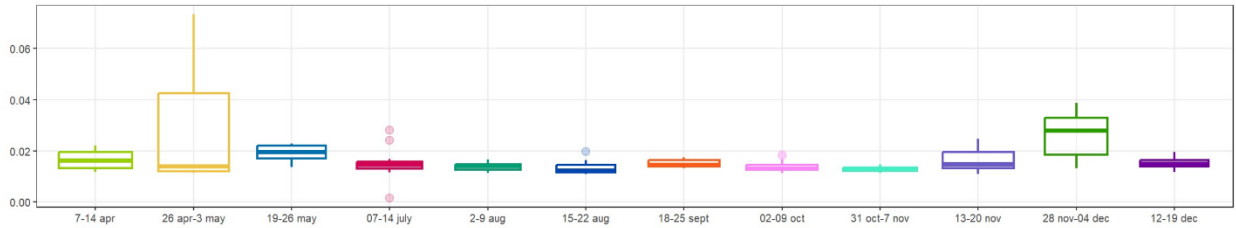
%SFe



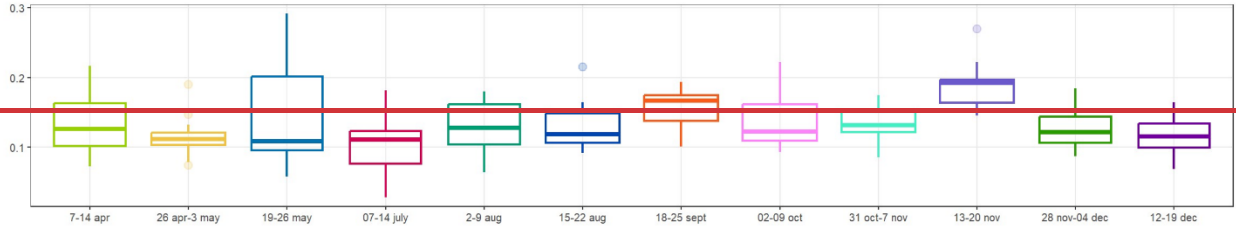
MSA



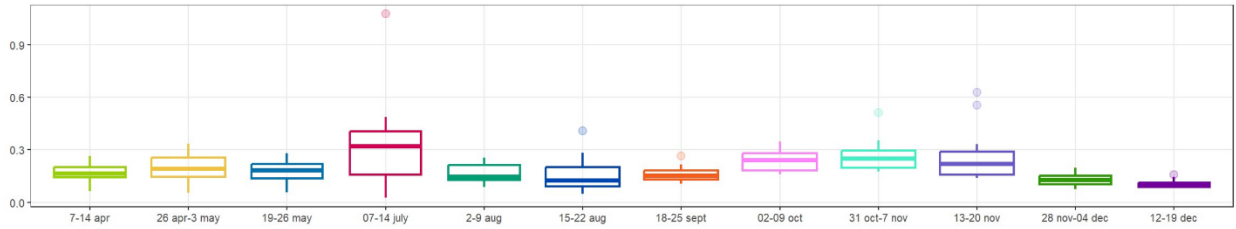
Formate



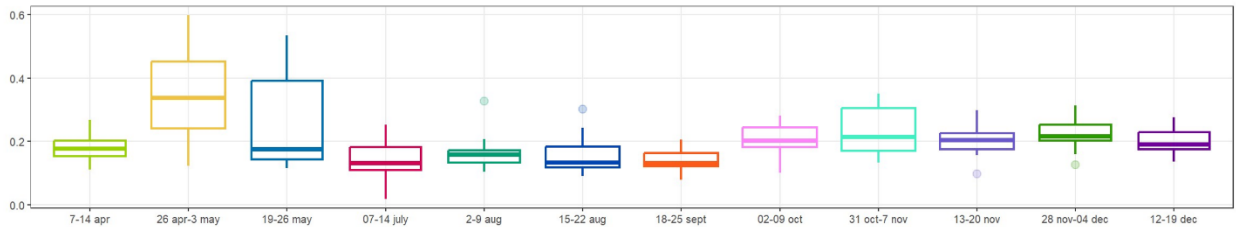
Oxalate



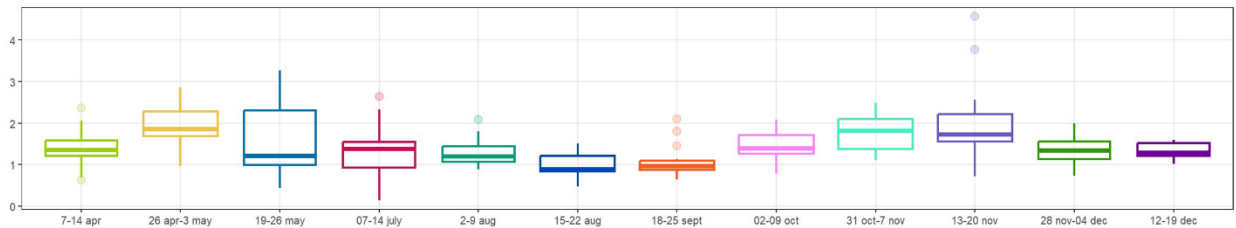
NO3

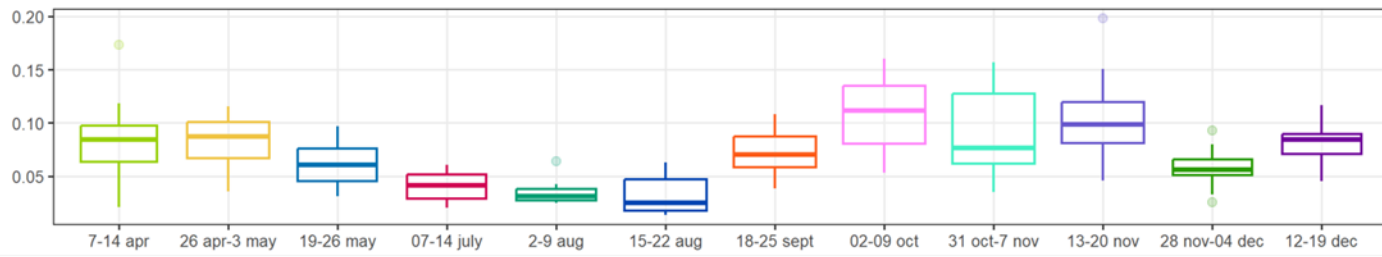
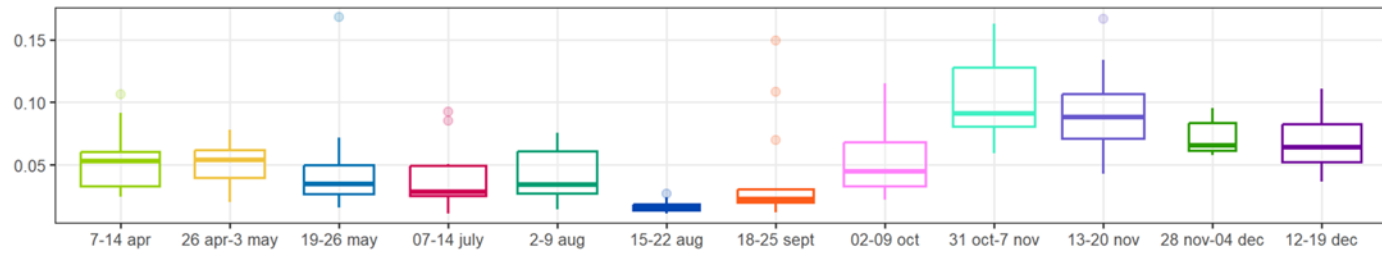
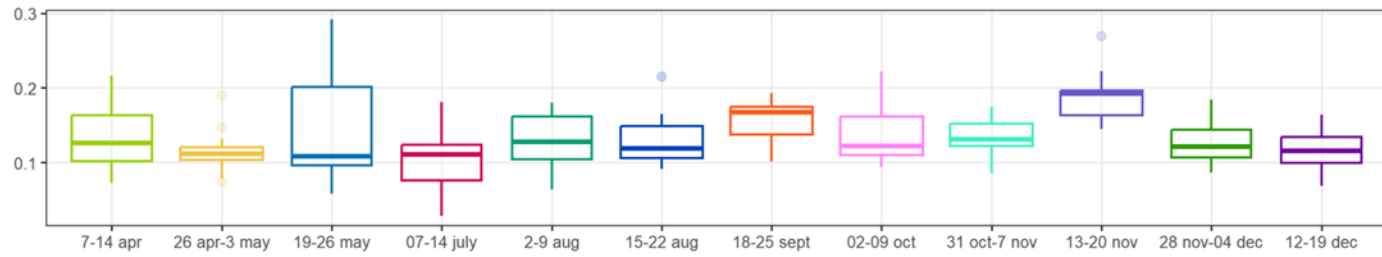
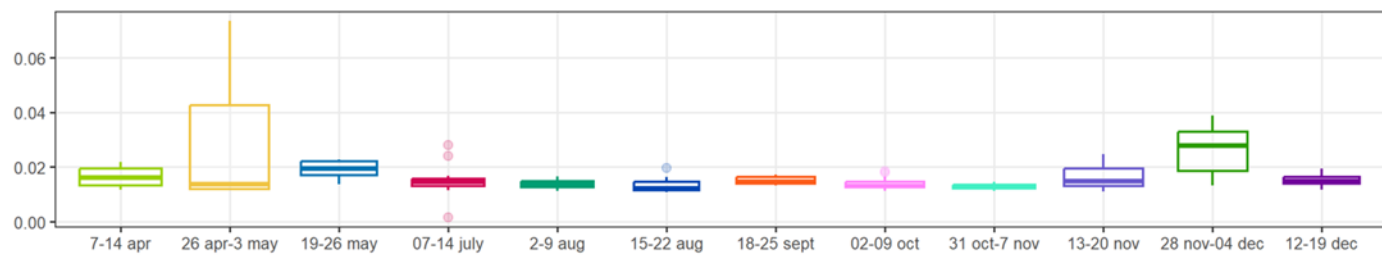
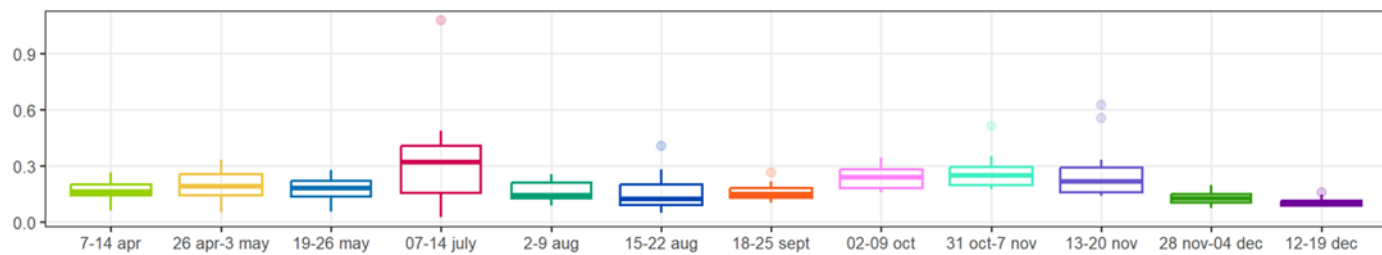
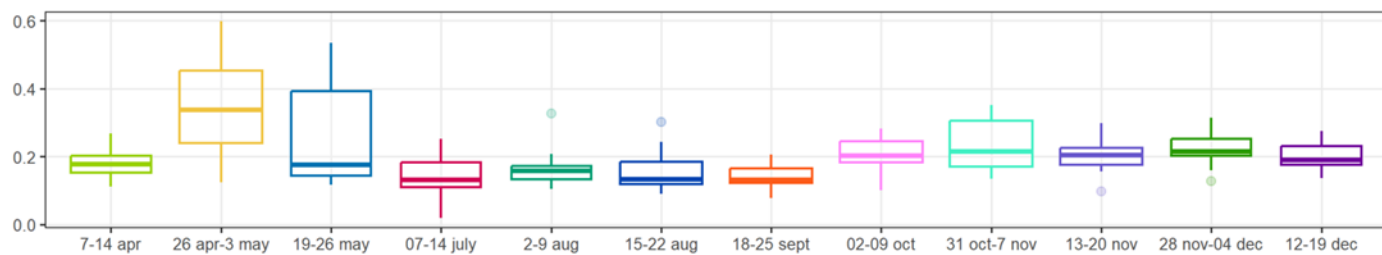
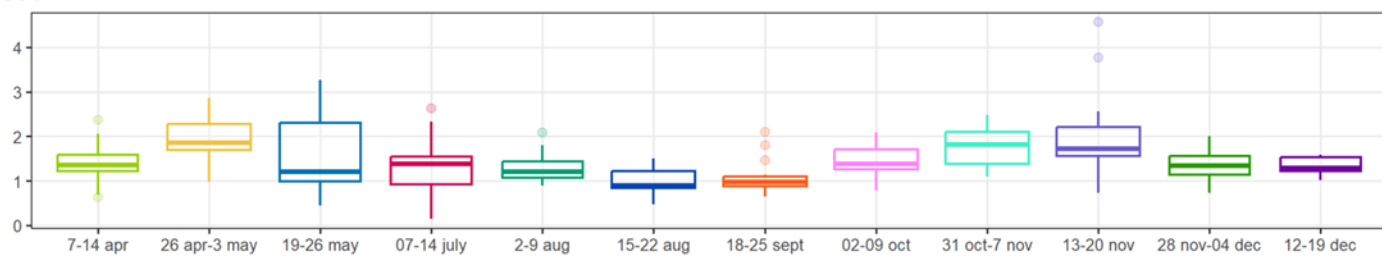


NH4



nssSO4



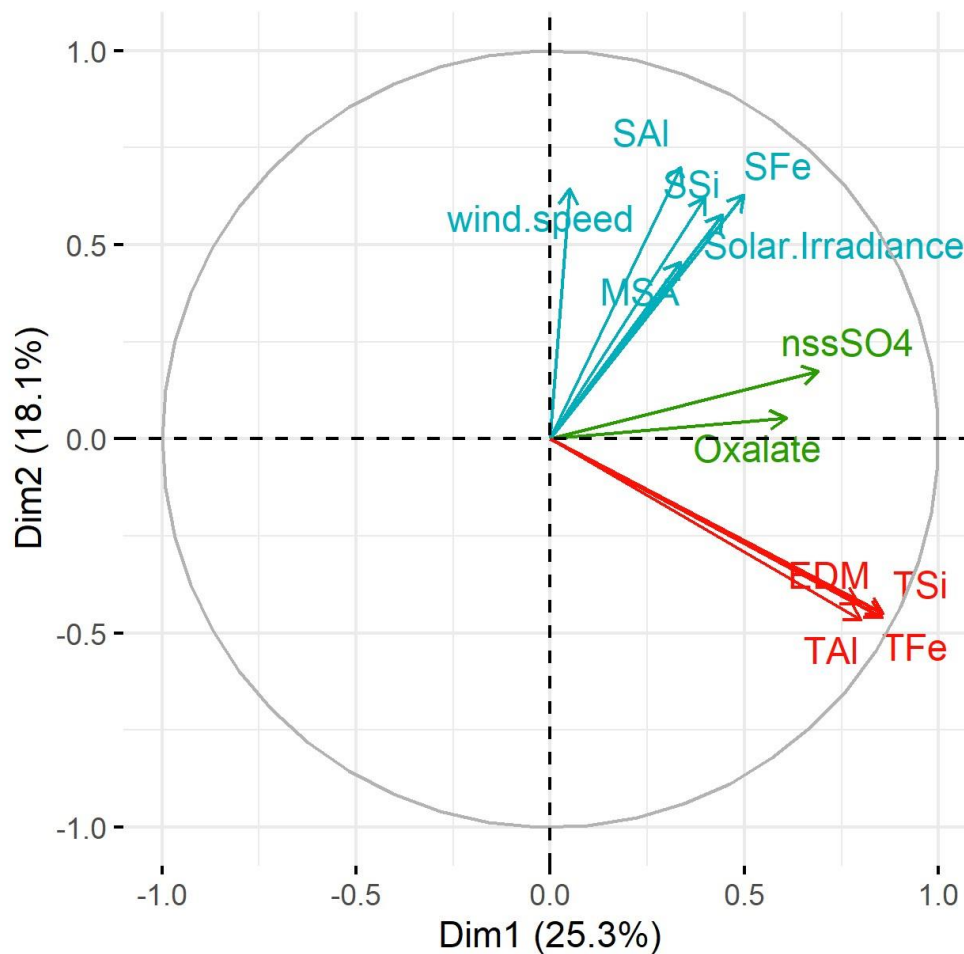
%SFe**MSA****Oxalate****Formate****NO3****NH4****nssSO4**

439 **Figure 6:** Box-plots of the averages of %SFe and secondary organic and inorganic compounds mass concentra-
440 tions ($\mu\text{g m}^{-3}$) for the sampling periods including all the samples (dust + background). Boxes and whiskers as in
441 Fig. 23.

442

443 The detailed time series of secondary compounds are shown in Fig. 6, where they are compared
444 to that of the %SFe iron fractional solubility. There is no clear seasonal cycle for any of the ionic com-
445 pounds, with the exception of MSA, which shows a similar time variability than %SFe. MSA concen-
446 trations were lowest between May and August (average $38.0 \pm 28.0 \text{ ng m}^{-3}$), while higher concentra-
447 tions were measured from September to December ($72.7 \pm 38.1 \text{ ng m}^{-3}$). These differences are also
448 observed for the dust cases only. The average MSA concentration was $40.6 \pm 23.4 \text{ ng m}^{-3}$ for Dust
449 04 to Dust 08 episodes. It increased to $77.7 \pm 35.3 \text{ ng m}^{-3}$, almost a factor of 2 between episodes
450 Dust 09 and Dust 13. The mass concentrations and the seasonal cycle of MSA are related with the
451 proximity of the strong coastal upwelling by the Benguela current (Formenti et al., 2019; KL20). The
452 maximum concentration of MSA (106.2 ng m^{-3}) was measured during episode Dust 11, which is also
453 the time of the highest SFe% observation. This episode was also characterised by the highest oxalate,
454 nss-SO_4^{2-} and NO_3^- concentrations. However, no clear correlation between the %SFe and the sec-
455 ondary compounds concentrations can be found in our data (Fig. S4). In order to statistically explore
456 the potential links between %SFe and various concentrations parameters, Figure 7 shows the
457 correspondence plot between total Fe, Al and Si, and their respective fractional solubility, the meas-
458 ured secondary compounds and the meteorological conditions during sampling obtained from Princi-
459 pal Component Analysis (PCA) for all the samples. The variables correlated in time are grouped to-
460 gether (the closer they are in the circle, the stronger the correlation) whereas the variables which are
461 anti-correlated are situated on the opposite side of the plot origin.

462



463 **Figure 7:** PCA analysis performed from the database including %SX,TX, EDM, secondary ions concentrations and
 464 meteorological parameters. The colour of variables by groups is defined by a clustering algorithm, tending to find
 465 clusters of comparable spatial extent. Each colour corresponds to a cluster of parameters which evolve in the same
 466 way. Formate, nitrate, ammonium, acetate, humidity, and wind speed are not visible in the plot showing that they
 467 are not significantly correlated with the other parameters (i.e. their squared cosine < 0.4).

468

469 The PCA plot (Fig. 7) emphasizes 3 groups of dependent parameters: 1. a high correlation between
 470 total Fe, Al and Si concentrations and dust loading (EDM), as previously identified in Table 1 and
 471 Fig. 3, 2. a relation between oxalate and nss-SO₄²⁻ concentrations, suggesting a common chemical
 472 process of formation, and 3. the dependence between %SFe (%SAI and %SSi), the MSA concentra-
 473 tions, the solar irradiance and to a lesser extent with the wind speed. While it is expected that the
 474 emission of mineral dust occurs when the wind speed is high, the correlation of %SFe with wind speed
 475 is rather surprising since the %SFe is independent of the dust load (Fig. 2 and 7). Figures S4 in the
 476 supplementary material present the plots between %SFe, MSA concentrations, solar irradiance and
 477 wind speed for background and dust events. The correlation between the wind speed and the MSA
 478 concentrations (Fig. S4) is consistent with Andreae et al. (1995), who demonstrated how, in this area
 479 due to persistent phytoplankton bloom, the atmospheric concentrations of dimethylsulphide (DMS),

480 the gaseous precursors of MSA, depend on the sea-to-air flux, in turn is determined by the concen-
481 trations in the ocean water and the surface wind speed.

482 As previously mentioned, Johansen and Key (2006) showed an increase of dissolution of ferrihydrite,
483 a proxy of iron(oxy)hydroxide found in desert mineral dust, by photolysis of the Fe(III)-MSIA (methane
484 sulfinic acid) complex, producing MSA and soluble Fe. Zhuang et al. (1992) proposed an increase of
485 iron dissolution by the acidification of aerosol particles associated with ~~dimethylsulphide (DMS)~~ oxi-
486 dation. Here, the link between the ~~%SFe iron fractional solubility~~, solar irradiance and MSA is in agree-
487 ment with the photo-reduction dissolution of Fe by MSA condensation on Fe-bearing dust. Thus, we
488 attribute the ~~%SFe iron fractional solubility~~ seasonality observed at HBAO both to solar irradiance and
489 MSA temporal evolution via this process. It is interesting to note that due to the high correlation be-
490 tween %SFe and %SAI and %SSi, the photochemical processes could also impact the solubility of all
491 element-bearing dust.

492 **4.3. Link to other sources of iron and oxalate**

493 Formenti et al. (2018) have shown that in the Austral winter, when the synoptic circulation is domi-
494 nantly anti-cyclonic, air masses laden with light-absorbing aerosols either from ship pollution or bio-
495 mass burning can be transported to HBAO (Formenti et al., 2018). However, the lowest Fe solubility
496 (< 5%) was measured in July and August 2017, and no correlation between the %SFe and the percent
497 mass fraction of iron from sources other than dust can be found in our data (not shown).

498 The mass apportionment of iron reported by KL20 indicates that, during the dust events and the
499 background periods, respectively, 7% and 29% of the mass of total elemental Fe was not associated
500 to mineral dust, but rather to a factor indicated as “ammonium-neutralised component”, mostly char-
501 acterised by secondary species, and non-sea-salt potassium (nss-K⁺). The PMF (Positive Matrix Fac-
502 torisation) analysis indicated that the “ammonium-neutralised component” was associated to photo-
503 oxidation of marine biogenic emission but also episodically to biomass burning. This component in-
504 cludes oxalate, the most concentrated organic species at HBAO, and the strongest of the organic
505 ligands promoting the photo-reduction of iron in mineral dust, henceforth the increase of its fractional
506 solubility (Paris and Desboeufs, 2013). Surprisingly, excepted individual cases (Dust 13), our analysis
507 does not show this strong link (Fig. 7), and indeed, contrary to the SFe%, the oxalate concentrations
508 measured at HBAO was practically constant with time (in average 0.14+/- 0.04 $\mu\text{g}\cdot\text{m}^{-3}$). The possible
509 pathways of oxalate formation in this complex atmosphere are numerous through the year, from nat-
510 ural and anthropogenic sources (marine, heavy-oil combustion, biomass burning) and in-cloud and
511 photo-oxidative processes (Baboukas et al., 2000; Myriokefalitakis et al., 2011).

512 **5. Concluding remarks**

513 For the first time, the fractional solubility of Fe in airborne atmospheric aerosols smaller than 10 μm
514 in diameter is investigated along the west coast of Namibia, in southern Africa, a critical region for the
515 global climate.

516 Ten intense episodes of transport of mineral dust from aeolian erosion were identified from the anal-
517 ysis of aerosol samples collected between May and December 2017 at the Henties Bay Aerosol Ob-
518 servatory (HBAO). Based on modelling and measurements, source regions were identified both in the
519 northern and southern gravel plains. Our data do not provide any evidence of the possible contribution
520 of dust from coastal riverbeds, which are considered to be frequent sources of atmospheric dust and
521 soluble iron in the region (Vickery et al., 2013; Von Holdt et al., 2017; Dansie et al., 2017a; 2017b).
522 The total iron represents, on average, 5.8 % (± 0.6 %) of the total dust mass, and that the average
523 water-soluble Fe fractional solubility is 6.9 % (± 3.3 %). These values should be useful to atmospheric
524 models estimating the dust-borne input of soluble Fe from the gravel plains in Namibia to the sur-
525 rounding oceans.

526 The seasonal increase of the ~~%SFe iron fractional solubility~~ is associated to that of the concentrations
527 of MSA and correlated to meteorological parameters such as the wind speed and the surface solar
528 irradiance. Our observations support the role of photo-chemical processes in the dissolution of Fe in
529 our samples, and suggest that the oxidation of the marine biogenic emissions from the northern Ben-
530 guela upwelling, favoured under high wind speed conditions, could play a significant role in increasing
531 the solubility of elemental iron in mineral dust aerosols over coastal Namibia. This is in agreement
532 with the mechanism described by Zhuang et al. (1992), who proposed an increase of iron dissolution
533 by the acidification of aerosol particles associated with DMS oxidation, and Johansen and Key (2006),
534 who showed an increase of dissolution of ferrihydrite, a proxy of iron(oxy)hydroxide found in desert
535 mineral dust, by photolysis of the Fe(III)-MSIA (methane sulfinic acid) complex, producing MSA and
536 soluble Fe. It is interesting to note that due to the high correlation between %SFe, ~~and~~ %SAI and
537 %SSi (and %STi), the same photochemical processes could also impact the solubility of all element-
538 bearing dust. The possible mechanism suggested by this paper could be responsible for initiating a
539 feedback loop whereby the input of dust of increased trace and major elements solubility would result
540 in stronger marine biogenic emissions to the atmosphere. This possible mechanism could increase
541 the iron solubility in mineral dust, maybe also initiating a feedback loop whereby the input of dust of
542 increased solubility would result in stronger marine biogenic emissions to the atmosphere, including
543 Volatile Organic Compounds (~~VOCs~~), in particular butene, massively emitted by the organisms in the
544 coastal marine foam (Giorio et al., 2022). This complex and dynamic environment where the interplay
545 between the input of atmospheric iron from transported dust and the marine biogenic emissions from
546 the Benguela oceanic upwelling system should be further addressed by future research.

547

548 **Data availability.** ~~Original and analysed data are available at the AERIS (<https://aerocio.aeris->~~
549 ~~[data.fr/project/](https://aerocio.aeris-data.fr/project/), last accessed 20/07/2023)~~ Atmospheric concentrations of total and dissolved ele-
550 ~~ments and water-soluble ions measured over coastal Namibia in 2017 are available in the Easy Data~~
551 ~~(Formenti et al., 2023, <https://doi.org/10.57932/2ac79cd1-282a-4004-87d5-38f0ebcaf40c>).~~ The sta-
552 tistical FactoMineR package is available in R (R version 4.1.2, 2021; [http://factominer.free.fr/in-](http://factominer.free.fr/index_fr.html)
553 ~~[dex_fr.html](http://factominer.free.fr/index_fr.html)~~, last accessed 20/07/2023). Meteorological data from the Wlotzkasbaken station
554 (22.31°S, 14.45°E, 73 m asl) are part of the Southern African Science Service Centre for Climate
555 Change and Adaptive Land Management (SASSCAL) ObservationNet (<https://www.sasscal.org/>; last
556 accessed 14/04/2023).

557

558 **Author contributions.** PF, DK, SJP, AN, MC, AF and SC prepared and performed the filter sampling.
559 RT, KD, PF, SC, ST, and CMB performed the XRF, IC and ICP analysis of the collected samples. BL
560 performed the field implementation. KS and SF performed the model calculations of dust emission
561 fluxes. JPC performed the model calculations of air mass back-trajectories. HA and JC provided with
562 the satellite retrieval of fog and low clouds. PF, KD, RT and SJP analysed and interpreted the dataset.
563 PF and KD wrote the paper with contributions from RT and SJP, and the remaining authors. PF and
564 SJP provided funding. PF coordinated the research activity and supervised its planning and execu-
565 tion.

566

567 **Competing interests.** PF is guest editor for the ACP Special Issue “New observations and related
568 modelling studies of the aerosol–cloud–climate system in the Southeast Atlantic and southern Africa
569 regions”. The remaining authors declare that they have no conflicts of interests.

570

571 **Special issue statement.** This article is part of the special issue “New observations and related mod-
572 elling studies of the aerosol–cloud–climate system in the Southeast Atlantic and southern Africa re-
573 gions (ACP/AMT inter-journal SI)”. It is not associated with a conference.

574

575 **Acknowledgements.** This work receives funding by the French Centre National de la Recherche
576 Scientifique (CNRS) and the South African National Research Foundation (NRF) through the
577 “Groupement de Recherche Internationale Atmospheric Research in southern Africa and the Indian
578 Ocean” (GDRI-ARSAIO) and the Project International de Coopération Scientifique (PICS) “Long-term
579 observations of aerosol properties in Southern Africa” (contract n. 260888) as well as by the Parte-
580 nariats Hubert Curien (PHC) PROTEA of the French Minister of Foreign Affairs and International De-
581 velopment (contract numbers 33913SF and 38255ZE). D. Klopper acknowledges the financial support

582 of the Climatology Research Group of North-West University and the travel scholarship of the French
583 Embassy in South Africa (internship at LISA in summer 2018). R. Torres-Sánchez acknowledges the
584 Postdoctoral Fellowship Margarita Alsolas (University of Huelva) funded by the Ministry of Universities
585 of Spain (NextGenerationEU). The Southern African Science Service Centre for Climate Change and
586 Adaptive Land Management (SASSCAL) ObservationNet (<https://www.sasscal.org/>) is acknowledged
587 for open-access data provision. The authors would also like to acknowledge the support by the IPGP
588 platform PARI for HR-ICP-MS analysis. F. Lahmidi and Z. Zeng (LISA) are acknowledged for support
589 to the ion chromatography analysis.

590

591 **References**

- 592 Andersen, H. and Cermak, J.: First fully diurnal fog and low cloud satellite detection reveals life cycle in the
593 Namib, *Atmos. Meas. Tech.*, 11, 5461–5470, doi: 10.5194/amt-11-5461-2018, 2018.
- 594 Andersen, H., Cermak, J., Solodovnik, I., Lelli, L. and Vogt, R.: Spatiotemporal dynamics of fog and low clouds
595 in the Namib unveiled with ground- and space-based observations, *Atmos. Chem. Phys.*, 1, 4383–4392, doi:
596 10.5194/acp-19-4383-2019, 2019.
- 597 Andersen, H., Cermak, J., Fuchs, J., Knippertz, P., Gaetani, M., Quinting, J., Sippel, S., and Vogt, R.: Synoptic-
598 scale controls of fog and low-cloud variability in the Namib Desert, *Atmos. Chem. Phys.*, 20, 3415–3438,
599 <https://doi.org/10.5194/acp-20-3415-2020>, 2020.
- 600 Andreae, M. O.: Soot Carbon and Excess Fine Potassium: Long-Range Transport of Combustion-Derived Aer-
601 osols, *Science*, 220, 1148-1151, doi:10.1126/science.220.4602.1148, 1983.
- 602 Andreae, M. O., Elbert, W., and de Mora, S. J.: Biogenic sulfur emissions and aerosols over the tropical South
603 Atlantic: 3. Atmospheric dimethylsulfide, aerosols and cloud condensation nuclei, *J. Geophys. Res.*, 100,
604 11335-11356, <https://doi.org/10.1029/94JD02828>, 1995.
- 605 Annegarn, H.J., van Grieken, R.E., Bibby, D.M. and von Blottnitz, F.: Background Aerosol Composition in the
606 Namib Desert, South West Africa (Namibia), *Atmos. Environ.*, 17, 2045–2053, doi: 10.1016/0004-
607 6981(83)90361-X, 1983.
- 608 Bhattachan, A., D'Odorico, P., Baddock, M.C., Zobeck, T.M., Okin, G.S., Cassar, N.: The Southern Kalahari: a
609 potential new dust source in the Southern hemisphere?, *Environ. Res. Lett.*, 7, 024001.
610 <http://dx.doi.org/10.1088/1748-9326/7/2/024001>, 2012.
- 611 Bhattachan, A., P. D'Odorico, and G. S. Okin, Biogeochemistry of dust sources in Southern Africa, *J. Arid En-
612 viron.*, 117, 18-27, <http://dx.doi.org/10.1016/j.jaridenv.2015.02.013>, 2015.
- 613 Baboukas, E. D., Kanakidou, M., and Mihalopoulos, N.: Carboxylic acids in gas and particulate phase above
614 the Atlantic Ocean, *J. Geophys. Res.*, 105, 14459–14471, <https://doi.org/10.1029/1999JD900977>, 2000.
- 615 Baker A.R., T. D. Jickells, M. Witt, and K. L. Linge, Trends in the solubility of iron, aluminium, manganese and
616 phosphorus in aerosol collected over the Atlantic Ocean., *Marine Chem.*, 98, 43-58,
617 <https://doi.org/10.1016/j.marchem.2005.06.004>, 2006.
- 618 Baker, A. R., and T. D. Jickells, Mineral particle size as a control on aerosol iron solubility, *Geophys. Res. Lett.*,
619 33, L17608. <https://doi.org/10.1029/2006GL026557>, 2006.
- 620 Baker, A. R., C. Adams C., T. G. Bell, T. D. Jickells, and L. Ganzeveld, Estimation of atmospheric nutrient inputs
621 to the Atlantic Ocean from 50°N to 50°S based on large-scale field sampling: iron and other dust-associated
622 elements, *Glob. Biogeochem. Cycles*, 27, 755–767, doi:10.1002/gbc.20062, 2013.
- 623 Baker, A. R., M. Thomas, H. W. Bange, and E. Plasencia Sánchez, E., Soluble trace metals in aerosols over
624 the tropical south-east Pacific offshore of Peru, *Biogeosciences*, 13, 817–825, [https://doi.org/10.5194/bg-13-](https://doi.org/10.5194/bg-13-817-2016)
625 817-2016, 2016.

626 Baker, Alex R., et T. D. Jickells, Atmospheric deposition of soluble trace elements along the Atlantic Meridional
627 Transect (AMT), in *The Atlantic Meridional Transect programme (1995-2016)* 158: 41-51.
628 <https://doi.org/10.1016/j.pocean.2016.10.002>, 2017.

629 Baker, A. R., M. Li, and R. Chance, Trace metal fractional solubility in size-segregated aerosols from the tropical
630 eastern Atlantic Ocean, *Global Biogeochemical Cycles*, 34, e2019GB006510.
631 <https://doi.org/10.1029/2019GB006510>, 2020.

632 Bryant, R. G., Bigg, G. R., Mahowald, N. M., Eckardt, F. D., and Ross, S. G., Dust emission response to climate
633 in southern Africa, *J. Geophys. Res.*, 112, D09207, doi:10.1029/2005JD007025, 2007.

634 Caponi, L., Formenti, P., Massabó, D., Di Biagio, C., Cazaunau, M., Pangui, E., Chevaillier, S., Landrot, G.,
635 Andreae, M. O., Kandler, K., Piketh, S., Saeed, T., Seibert, D., Williams, E., Balkanski, Y., Prati, P., and
636 Doussin, J.-F.: Spectral- and size-resolved mass absorption efficiency of mineral dust aerosols in the
637 shortwave spectrum: a simulation chamber study, *Atmos. Chem. Phys.*, 17, 7175–7191,
638 <https://doi.org/10.5194/acp-17-7175-2017>, 2017.

639 Chaboureau, J.-P., L. Labbouz, C. Flamant, and A. Hodzic. Acceleration of the southern African easterly jet
640 driven by radiative effect of biomass burning aerosols and its impact on transport during AEROCLO-sA, *At-*
641 *mos. Chem. Phys.*, 22, 8639-8658, <https://doi.org/10.5194/acp-22-8639-2022>, 2022.

642 Chance R, T. D. Jickells and A. R. Baker, Atmospheric trace metal concentrations, solubility and deposition
643 fluxes in remote marine air over the south-east Atlantic, *Marine Chemistry*, 177, 45–56, doi:10.1016/j.mar-
644 *chem.2015.06.028*, 2015.

645 Dansie, A. P., G. F. S. Wiggs, D. S. G. Thomas, and R. Washington, Measurements of windblown dust charac-
646 teristics and ocean fertilisation potential: The ephemeral river valleys of Namibia, *Aeolian Res.*, 29, 30–41,
647 doi:10.1016/j.aeolia.2017.08.002, 2017a.

648 Dansie, A. P., G. F. S. Wiggs, and D. S. G. Thomas, Iron and nutrient content of wind-erodible sediment in the
649 ephemeral river valleys of Namibia, *Geomorphology*, 290, 335-346, <https://doi.org/10.1016/j.geomorph.2017.03.016>, 2017b.

651 Dansie AP, Thomas DSG, Wiggs GFS, Baddock MC, Ashpole I. Plumes and blooms - Locally-sourced Fe-rich
652 aeolian mineral dust drives phytoplankton growth off southwest Africa. *Sci Total Environ.*, doi: 10.1016/j.sci-
653 *totenv.2022.154562*, 2022.

654 Desboeufs, K. V., R. Losno, et J. L. Colin, Factors influencing aerosol solubility during cloud processes, *Atmos.*
655 *Environ.*, 35, 3529-3537, [https://doi.org/10.1016/S1352-2310\(00\)00472-6](https://doi.org/10.1016/S1352-2310(00)00472-6), 2001.

656 Desboeufs, K.V., Sofikitis, A., Losno, R., Colin, J.L., Ausset, P. Dissolution and solubility of trace metals from
657 natural and anthropogenic aerosol particulate matter, *Chemosphere* 58, 195–203, 2005.

658 Desboeufs, K., Fu, Y., Bressac, M., Tovar-Sánchez, A., Triquet, S., Doussin, J.F., Giorio, C., Chazette, P.,
659 Disnaquet, J., Feron, A., Formenti, P., Maisonneuve, F., Rodríguez-Romero, A., Zapf, P., Dulac, F., and
660 Guieu, C., Wet deposition in the remote western and central Mediterranean as a source of trace metals to
661 surface seawater, *Atmos. Chem. Phys.*, 22, 2309–2332, <https://doi.org/10.5194/acp-22-2309-2022>, 2022.

662 Eltayeb, M.A.; Van Grieken, R.E., Maenhaut, W. and Annegarn, H.J.: Aerosol-Soil Fractionation for Namib De-
663 sert Samples. *Atmos. Environ.*, 27(5), [https://doi.org/10.1016/0960-1686\(93\)90185-2](https://doi.org/10.1016/0960-1686(93)90185-2), 1993.

664 Feuerstein, S., and Schepanski, K.: Identification of Dust Sources in a Saharan Dust Hot-Spot and Their Imple-
665 mentation in a Dust-Emission Model, *Remote Sensing*, 11, doi:10.3390/rs110100004, 2019.

666 Flamant, C., M. Gaetani, J.-P. Chaboureau, P. Chazette, S. J. Piketh, and P. Formenti. Smoke in the river: an
667 Aerosols, Radiation and Clouds in southern Africa (AEROCLO-SA) case study, *Atmos. Chem. Phys.*, 22,
668 5701–5724, <https://doi.org/10.5194/acp-22-5701-2022>, 2022.

669 Formenti, P., Schütz, L., Balkanski, Y., Desboeufs, K., Ebert, M., Kandler, K., Petzold, A., Scheuven, D.,
670 Weinbruch, S., and Zhang, D.: Recent progress in understanding physical and chemical properties of African
671 and Asian mineral dust, *Atmos. Chem. Phys.*, 11, 8231–8256, <https://doi.org/10.5194/acp-11-8231-2011>,
672 2011.

673 Formenti, P., S. Caquineau, K. Desboeufs, A. Klaver, S. Chevallier, E. Journet, J. L. Rajot, Mapping the phys-
674 ico-chemical properties of mineral dust in western Africa: mineralogical composition, *Atmos. Chem. Phys.*, 14,
675 10663-1068, 2014.

676 Formenti, P., Piketh, S. J., Namwoonde, A., Klopper, D., Burger, R., Cazaunau, M., Feron, A., Gaimoz, C.,
677 Broccardo, S., Walton, N., Desboeufs, K., Siour, G., Hanghome, M., Mafwila, S., Omoregie, E., Junkermann,
678 W., and Maenhaut, W.: Three years of measurements of light-absorbing aerosols over coastal Namibia: sea-
679 sonality, origin, and transport, *Atmos. Chem. Phys.*, 18, 17003-17016, [https://doi.org/10.5194/acp-18-17003-](https://doi.org/10.5194/acp-18-17003-2018)
680 2018, 2018.

681 Formenti, P., B. D'Anna, C. Flamant, M. Mallet, S.J. Piketh, K. Schepanski, F. Waquet, F. Auriol, G. Brogniez,
682 F. Burnet, J. Chaboureau, A. Chauvigné, P. Chazette, C. Denjean, K. Desboeufs, J. Doussin, N. Elguindi, S.
683 Feuerstein, M. Gaetani, C. Giorio, D. Klopper, M.D. Mallet, P. Nabat, A. Monod, F. Solmon, A. Namwoonde,
684 C. Chikwililwa, R. Mushi, E.J. Welton, and B. Holben, The Aerosols, Radiation and Clouds in Southern Africa
685 Field Campaign in Namibia: Overview, Illustrative Observations, and Way Forward, *Bull. Amer. Meteor. Soc.*,
686 100, 1277–1298, <https://doi.org/10.1175/BAMS-D-17-0278.1>, 2019.

687 Gao, Y., Xu, G., Zhan, J., Zhang, J., Li, W., Lin, Q., Chen, L., and Lin, H., Spatial and particle size distributions
688 of atmospheric dissolvable iron in aerosols and its input to the Southern Ocean and coastal East Antarctica,
689 *J. Geophys. Res.*, 118, 12,634–12,648, doi:10.1002/2013JD020367, 2013.

690 Gili, S., Vanderstraeten, A., Chaput, A., King, J., Gaiero, D. M., Delmonte, B., Vallelonga, Paola Formenti,
691 Claudia Di-Biagio, Mathieu Cazaunau, Edouard Pangui, Jean-Francois Doussin, Mattielli, N., South African
692 dust contribution to the high southern latitudes and East Antarctica during interglacial stages, *Communications*
693 *Earth & Environment*, 3, 129, <https://doi.org/10.1038/s43247-022-00464-z>, 2022.

694 Ginoux, P., Prospero, J.M., Gill, T.E., Hsu, N.C., Zhao, M.: Global-scale attribution of anthropogenic and natural
695 dust sources and their emission rates based on MODIS Deep Blue aerosols products, *Rev. Geophys.*, 50,
696 RG3005, doi:10.1029/2012RG000388, 2012.

697 Giorio, C., Doussin, J.F., D'Anna, B., Mas, S., Filippi, D., Denjean, C., Mallet, M.D., Bourriane, T., Burnet, F.,
698 Cazaunau, M., Chikwililwa, C., Desboeufs, K., Feron, A., Michoud, V., Namwoonde, A., Andreae, M.O., Piketh,

699 S.J. and Formenti, P.: Butene emissions from coastal ecosystems may contribute to new particle formation,
700 *Geophys. Res. Lett.*, 49, <https://doi.org/10.1029/2022GL098770>, 2022.

701 Grini, A., Tulet, P., and Gomes, L.: Dusty weather forecasts using the MesoNH mesoscale atmospheric model.
702 *J. Geophys. Res.*, 111, D19205, <https://doi.org/10.1029/2005JD007007>, 2006.

703 Hamilton, D. S., Perron, M.M.G., Bond, T.C., Bowie, A.R., Buchholz, R.R., Guieu, C., Ito, A., Maenhaut, W.,
704 Myriokefalitakis, S., Olgun, N., Rathod, S.D., Schepanski, K., Tagliabue, A., Wagner, R. and Mahowald, N.M.:
705 Earth, wind, fire, and pollution: Aerosol nutrient sources and impacts on ocean biogeochemistry, *Annual re-*
706 *view of Marine Science*, 14, pp. 303- 330, <https://doi.org/10.1146/annurev-marine-031921-013612>, 2021.

707 Heike, K and J. Volkel, Soil clay minerals in Namibia and their significance for the terrestrial and marine past
708 global change, *African Study Monographs, Suppl.40*, 2010.

709 Heimbürger, A., Losno, R., and Triquet, S.: Solubility of iron and other trace elements in rainwater collected on
710 the Kerguelen Islands (South Indian Ocean), *Biogeosciences*, 10, 6617–6628, [https://doi.org/10.5194/bg-10-](https://doi.org/10.5194/bg-10-6617-2013)
711 [6617-2013](https://doi.org/10.5194/bg-10-6617-2013), 2013.

712 Hooper, H., Mayewski, P., Marx, S., Henson, S., Potocki, M., Sneed, S., Handley, M., Gasso, S., Fischer, M.,
713 Saunders, K.M., Examining links between dust deposition and phytoplankton response using ice cores. *Aeo-*
714 *lian Res.*, 36, 45-60, <https://doi.org/10.1016/j.aeolia.2018.11.001>, 2019.

715 Ito, A., and Kok, J. F.: Do dust emissions from sparsely vegetated regions dominate atmospheric iron supply to
716 the Southern Ocean?, *J. Geophys. Res.*, 122, 3987-4002, <https://doi.org/10.1002/2016JD025939>, 2017.

717 Ito, A., Y. Ye, C. Baldo, and Z. Shi, Ocean Fertilization by Pyrogenic Aerosol Iron. *npj Climate Atmos. Sci.*, 4,
718 30, doi: 10.1038/s41612-021-00185-8, 2021.

719 Jickells, T., Andersen, K.K., Baker, A., Bergametti, G., Brooks, N., Cao, J., Boyd, P., Duce, R., Hunter, K.,
720 Global iron connections between desert dust, ocean biogeochemistry, and climate, *Science*, 308, 67-71, DOI:
721 10.1126/science.1105959, 2005.

722 Journet, E., Desboeufs, K., Caquineau, S. and Colin, J. L.: Mineralogy as a critical factor of dust iron solubility,
723 *Geophys. Res. Lett.*, 35, <https://doi.org/10.1029/2007GL031589>, 2008.

724 Johansen, A. M., and Key, J. M.: Photoreductive dissolution of ferrihydrite by methanesulfinic acid: Evidence of
725 a direct link between dimethylsulfide and iron-bioavailability, *Geophys. Res. Lett.*, 33, L14818,
726 doi:10.1029/2006GL026010, 2006.

727 Kaplan, J.O., Bigelow, N.H., Prentice, I.C., Harrison, S.P., Bartlein, P.J., Christensen, T.R., Cramer, W., Matve-
728 yeva, N.V., McGuire, A.D., Murray, D.F., Razzhivin, V.Y., Smith, B., Walker, D.A., Anderson, P.M., Andreev,
729 A.A., Brubaker, L.B., Edwards, M.E. and Lozhkin A.V.: Climate change and Arctic ecosystems: 2. Modeling,
730 paleodata-model comparison and future projections, *J. Atmos. Res.*, 108, 8171, doi: 10.1029/2002JD002559,
731 2003.

732 Kanguuehi, K. I., Southern African dust characteristics and potential impacts on the surrounding oceans, PhD
733 Thesis, Stellenbosch University, <http://hdl.handle.net/10019.1/123923>, 2021.

734 Klopfer, D., Formenti, P., Namwoonde, A., Cazaunau, M., Chevaillier, S., Feron, A., Gaimoz, C., Hease, P.,
735 Lahmidi, F., Mirande-Bret, C., Triquet, S., Zeng, Z. And Piketh, S.J.: Chemical composition and source apportionment of atmospheric aerosols on the Namibian Coast, *Atmos. Chem. Phys.*, 20, pp. 15811 – 15833,
736 <https://doi.org/10.5194/acp-20-15811-2020>, 2020.

738 Kok, J. F., Albani, S., Mahowald, N. M., and Ward, D. S.: An improved dust emission model – Part 2: Evaluation
739 in the Community Earth System Model, with implications for the use of dust source functions, *Atmos. Chem. Phys.*, 14, 13043–13061, <https://doi.org/10.5194/acp-14-13043-2014>, 2014.

741 Kok, J.F., Ridley, D.A., Zhou, Q., Miller, R.L., Zhao, C., Heald, C.L., Ward, D.S., Albani, S., Haustein, K.: Smaller
742 desert dust cooling effect estimated from analysis of dust size and abundance. *Nature Geoscience*, 10, 274–
743 278, <https://doi.org/10.1038/ngeo2912>, 2017.

744 Laurent, B., Marticorena, B., Bergametti, G., Chazette, P., Maignan, F. and Schmechtig C.: Simulation of the
745 mineral dust emission frequencies from desert areas of China and Mongolia using an aerodynamic roughness
746 length map derived from POLDER/ADEOS 1 surface products, *J. Geophys. Res.*, 110, D18, doi:
747 10.1029/2004JD005013, 2005.

748 Lide, D. R.: *CRC Handbook of Chemistry and Physics 1991–1992*, CRC Press, Boca Raton, Florida, 1992.

749 Liu, M., Matsui, H., Hamilton, D.S., Lamb, K.D., Rathod, S.D., Schwarz, J.P. and Mahowald, N.M.: The underap-
750 preciated role of anthropogenic sources in atmospheric soluble iron flux to the Southern Ocean, *Climate At-
751 mos. Sci.*, 5, 28, <https://doi.org/10.1038/s41612-022-00250-w>, 2022.

752 Longo, A., F. Y. Feng, B., W. M. Landing, R.U. Shelley, A. Nenes, N. Mihalopoulos, K. Violaki, E. D. Ingall.
753 Influence of Atmospheric Processes on the Solubility and Composition of Iron in Saharan Dust, *Environ. Sci.
754 Tech.*, 50, 13: 6912-20. <https://doi.org/10.1021/acs.est.6b02605>, 2016.

755 Mahowald, N., Luo, C., del Corral, J., Zender, C.S.: Interannual variability in atmospheric mineral aerosols from
756 a 22-year model simulation and observational data, *J. Geophys. Res.*, 108 (D12),
757 <https://doi.org/10.1029/2002JD002821>, 2003.

758 Marcotte, A.R., Anbar, A.D., Majestic, B.J., Herckes, P.: Mineral dust and iron solubility: Effects of composition,
759 particle size, and surface area, *Atmosphere*, 11, 533, doi:10.3390/atmos11050533, 2020.

760 Marticorena, B. and Bergametti, G.: Modelling the atmospheric dust cycle: 1. Design of a soil-derived dust
761 emission scheme, *J. Geochem. Res.*, 16415-16430, 1995.

762 Marticorena, B., Chazette, P., Bergametti, G., Dulac, F., Legrand, M.: Mapping the aerodynamic roughness
763 length of desert surfaces from the POLDER/ADEOS bi-directional reflectance product, *Int. J. Remote Sens.*,
764 25, 603– 626, 2004.

765 Myriokefalitakis, S., Tsigaridis, K., Mihalopoulos, N., Sciare, J., Nenes, A., Kawamura, K., Segers, A., and
766 Kanakidou, M.: In-cloud oxalate formation in the global troposphere: a 3-D modeling study, *Atmos. Chem.
767 Phys.*, 11, 5761-5782, doi:10.5194/acp-11-5761-2011, 2011.

768 Paris, R., Desboeufs, K. V., Formenti, P., Nava, S., and Chou, C.: Chemical characterisation of iron in dust and
769 biomass burning aerosols during AMMA-SOP0/DABEX: implication for iron solubility, *Atmos. Chem. Phys.*,
770 10, 4273–4282, <https://doi.org/10.5194/acp-10-4273-2010>, 2010.

771 Paris, R., K.V. Desboeufs, et E. Journet. Variability of dust iron solubility in atmospheric waters: Investigation of
772 the role of oxalate organic complexation, *Atmos. Environ.*, 45, 6510-17. <https://doi.org/10.1016/j.atmosenv.2011.08.068>, 2011.

774 Paris, R., and K. V. Desboeufs, Effect of atmospheric organic complexation on iron-bearing dust solubility. *Atmos. Chem. Phys.*, 13, 4895-4905, <https://doi.org/10.5194/acp-13-4895-2013>, 2013.

776 Perron, M. M. G., Strzelec, M., Gault-Ringold, M., Proemse, B. C., Boyd, P. W., and Bowie, A. R.: Assessment
777 of leaching protocols to determine the solubility of trace metals in aerosols, *Talanta*, 208, 120377,
778 <https://doi.org/10.1016/j.talanta.2019.120377>, 2020.

779 Prospero, J.M., Ginoux, P., Torres, O., Nicholson S.E. and Gill, T.M.: Environmental characterization of global
780 sources of atmospheric soil dust identified with the Nimbus 7 total ozone mapping spectrometer (TOMS) ab-
781 sorbing aerosol product. *Reviews of Geophysics*, 40 (1): 1002, <https://doi.org/10.1029/2000RG000095>, 2002.

782 Redemann, J., Wood, R., Zuidema, P., Doherty, S. J., Luna, B., LeBlanc, S. E., Diamond, M. S., Shinozuka, Y.,
783 Chang, I. Y., Ueyama, R., Pfister, L., Ryoo, J.-M., Dobracki, A. N., da Silva, A. M., Longo, K. M., Kacenelen-
784 bogen, M. S., Flynn, C. J., Pistone, K., Knox, N. M., Piketh, S. J., Haywood, J. M., Formenti, P., Mallet, M.,
785 Stier, P., Ackerman, A. S., Bauer, S. E., Fridlind, A. M., Carmichael, G. R., Saide, P. E., Ferrada, G. A., Howell,
786 S. G., Freitag, S., Cairns, B., Holben, B. N., Knobelspiesse, K. D., Tanelli, S., L'Ecuyer, T. S., Dzambo, A. M.,
787 Sy, O. O., McFarquhar, G. M., Poellot, M. R., Gupta, S., O'Brien, J. R., Nenes, A., Kacarab, M., Wong, J. P.
788 S., Small-Griswold, J. D., Thornhill, K. L., Noone, D., Podolske, J. R., Schmidt, K. S., Pilewskie, P., Chen, H.,
789 Cochrane, S. P., Sedlacek, A. J., Lang, T. J., Stith, E., Segal-Rozenhaimer, M., Ferrare, R. A., Burton, S. P.,
790 Hostetler, C. A., Diner, D. J., Seidel, F. C., Platnick, S. E., Myers, J. S., Meyer, K. G., Spangenberg, D. A.,
791 Maring, H., and Gao, L.: An overview of the ORACLES (ObseRvations of Aerosols above CLouds and their
792 intEractionS) project: aerosol–cloud–radiation interactions in the southeast Atlantic basin, *Atmos. Chem.*
793 *Phys.*, 21, 1507–1563, <https://doi.org/10.5194/acp-21-1507-2021>, 2021.

794 Reichholf, J. H., Is Saharan Dust a Major Source of Nutrients for the Amazonian Rain Forest?, *Studies on*
795 *Neotropical Fauna and Environment*, 21:4, 251-255, DOI: 10.1080/01650528609360710, 1986.

796 Rodríguez, S., Prospero, J.M., Lopez-Darias, J., Garcia-Alvarez, M.I., Zuidema, P., Nava, S., Lucarelli, F., Gas-
797 ton, C.J., Galindo, L., Sosa, E.: Tracking the changes of iron solubility and air pollutants traces as African dust
798 transits the Atlantic in the Saharan dust outbreaks. *Atmos. Environ.*, 246, 118092, <https://doi.org/10.1016/j.atmosenv.2020.118092>, 2021.

800 Rodríguez, S., Riera, R., Fonteneau, A., Alonso-Pérez, S., and López-Darias, J.: African desert dust influences
801 migrations and fisheries of the Atlantic skipjack-tuna, *Atmospheric Environment*, 312, 120022,
802 <https://doi.org/10.1016/j.atmosenv.2023.120022>, 2023.

803 Shelley, R.U., Morton, P.L., Landing, W.M., Elemental ratios and enrichment factors in aerosols from the US-
804 GEOTRACES North Atlantic transects. *Deep-Sea Res. II*, 2014.

805 Shelley, R. U., Landing, W. M., Ussher, S. J., Planquette, H., & Sarthou, G. Regional trends in the fractional
806 solubility of Fe and other metals from North Atlantic aerosols (GEOTRACES cruises GA01 and GA03) follow-
807 ing a two-stage leach, *Biogeosciences*, 15(8), 2271–2288. <https://doi.org/10.5194/bg-15-2271-2018>, 2018.

808 Sholkovitz, E.R., Sedwick, P.N., Church, T.M. Influence of anthropogenic combustion emissions on the deposi-
809 tion of soluble aerosol iron to the ocean: empirical estimates for island sites in the North Atlantic, *Geochim.*
810 *Cosmochim. Acta*, 73, 3981–4003, <http://dx.doi.org/10.1016/j.gca.2009.04.029>, 2009.

811 Siefert, R. L., S. O. Pehkonen, Y. Erel, and M. R. Hoffman, Iron photochemistry of aqueous suspensions of
812 ambient aerosol with added organic acids, *Geochim. Cosmochim. Acta*, 58, 3271–3279, 1994.

813 Spirig, R., Vogt, R., Larsen, J. A., Feigenwinter, C., Wicki, A., Franceschi, J., Parlow, E., Adler, B., Kalthoff, N.,
814 Cermak, J., Andersen, H., Fuchs, J., Bott, A., Hacker, M., Wagner, N., Maggs-Kölling, G., Wassenaar, T. and
815 Seely, M.: Probing the fog life-cycles in the Namib desert, *Bull. Am. Met. Soc.*, 100, 2491-2508,
816 [doi:10.1175/bams-d-18-0142.1](https://doi.org/10.1175/bams-d-18-0142.1), 2019.

817 Swan, H.B., and J. P. Ivey, Elevated particulate methanesulfonate, oxalate and iron over Sydney Harbour in the
818 austral summer of 2019-20 during unprecedented bushfire activity, *Atmos. Environ.*, 226, 118739,
819 <https://doi.org/10.1016/j.atmosenv.2021.118739>, 2021.

820 Swap, R., Garstang, M., Macko, S.A., et al., The long-range transport of southern African aerosols to the tropical
821 South Atlantic. *J. Geophys. Res.*, 101, 23777–23791, <https://doi.org/10.1029/95jd01049>, 1996.

822 Takahashi, Y., Higashi, M., Fukurawa, T., Mitsunobu, S.: Change of iron species and iron solubility in Asian
823 dust during the long-range transport from western China to Japan, *Atmos. Chem. Phys*, 11, 11237-11252,
824 [doi:10.5194/acp-11-11237-2011](https://doi.org/10.5194/acp-11-11237-2011), 2011.

825 Tao, Y., Murphy, J.G.: The mechanisms responsible for the interactions among oxalate, pH, and Fe dissolution
826 in PM_{2.5}. *Earth and Space Chemistry*, 3, 2259-2265, <https://doi.org/10.1021/acsearthspacechem.9b00172>,
827 2019.

828 Tegen, I., Schepanski, K.: The Global distribution of Mineral Dust, *IOP Conference Series: Earth and Environ-*
829 *mental Sciences*, 7, 012001, [doi:10.1088/1755-1307/7/1/012001](https://doi.org/10.1088/1755-1307/7/1/012001), 2009.

830 Tyson, P. D. and Preston-Whyte, R. A.: *The Weather and Climate of Southern Africa*, 2nd ed., Oxford University
831 Press Southern Africa, Cape Town, 2014.

832 Ventura, A., Simões, E.F.C., Almeida, A.S., Martins, R., Duarte, A.C., Loureiro, S., Duarte, R.M.B.O., Deposition
833 of aerosols onto upper ocean and their impacts on marine biota, *Atmosphere*, 12, 684,
834 <https://doi.org/10.3390/atmos12060684>, 2021.

835 Vickery, K.J., Eckardt, F.D.: Dust emission controls on the lower Kuiseb River valley, Central Namib, *Aeolian*
836 *Res.*, 10, 125-133, <https://doi.org/10.1016/j.aeolia.2013.02.006>, 2013.

837 von Holdt, J.R., Eckardt, F.D., Wiggs, G.F.S.: Landsat identifies aeolian dust emission dynamics at the landform
838 scale, *Remote Sensing Environ.*, 198, 229-243, <https://doi.org/10.1016/j.rse.2017.06.010>, 2017.

839 Wozniak, A. S.; Shelley, R. U.; Sleighter, R. L.; Abdulla, H. A. N.; Morton, P. L.; Landing, W. M.; Hatcher, P. G.
840 Relationships among aerosol water soluble organic matter, iron and aluminium in European, North African,

841 and Marine air masses from the 2010 US GEOTRACES cruise, *Mar. Chem.*, 154, 24– 33 DOI: 10.1016/j.mar-
842 chem.2013.04.011, 2013.

843 Wozniak, A. S., R.U. Shelley, S.D. McElhenie, W.M. Landing, P. G. Hatcher. Aerosol water soluble organic
844 matter characteristics over the North Atlantic Ocean: Implications for iron-binding ligands and iron solubility.
845 SCOR WG 139: Organic Ligands – A Key Control on Trace Metal Biogeochemistry in the Ocean 173: 162-72.
846 <https://doi.org/10.1016/j.marchem.2014.11.002>, 2015.

847 Zhuang, G., Z. Yi, R. A. Duce, and Brown, P.R.: Link between iron and sulphur cycles suggested by detection
848 of Fe (II) in remote marine aerosols, *Nature*, 355, pp. 537–539, <https://doi.org/10.1038/355537a0>, 1992.

849

850